



# Spring-in of composite L-shape specimens: An experimental and numerical investigation

Neoklis Traiforos<sup>a,b,\*</sup>, Mikhail Matveev<sup>b</sup>, Dimitrios Chronopoulos<sup>c</sup>, Thomas Turner<sup>b</sup>

<sup>a</sup> Airbus Defence and Space GmbH, Rechliner Str., 85077, Manching, Germany

<sup>b</sup> The University of Nottingham, Faculty of Engineering, Polymer Composites Research Group, Advanced Manufacturing Building, 522 Derby Rd, Nottingham NG8 1BB, United Kingdom

<sup>c</sup> KU Leuven, Department of Mechanical Engineering and Mecha(tro)nic System Dynamics (LMSD), 9000, Belgium

## ARTICLE INFO

### Keywords:

Process induced distortion  
Thermoset composite materials  
Finite element analysis (FEA)  
Process simulation  
Dimensional control

## ABSTRACT

The effect of stacking sequence, specimen thickness, tooling material and curing cycle on process induced distortions of L-shape composite structures is investigated experimentally and numerically. Sixty specimens were manufactured, and their spring-in angle was compared against simulation and analytical results. A thermo-chemo-mechanical simulation approach was developed to simulate the experiment by employing a modified Cure Hardening Instantaneously Linear Elastic (CHILE) and a linear viscoelastic material model. Freestanding, fixed and contact boundary conditions were investigated. The spring-in angle of the parts predicted by the modified CHILE material model, was found to be higher than that predicted by the viscoelastic model. The tool material significantly affects the distortion of the parts and contact boundary conditions should be employed for an accurate prediction of the part shape. Balanced, symmetric and thick laminates contribute to a reduction in part distortion, while elevated curing temperatures slightly affect the distortion level of the parts.

## 1. Introduction

Process Induced Distortions (PID) are inevitably present in composite structures. Regardless of the process, resin infusion, automatic tape placement etc., residual stresses are induced in the structure leading to a deviation from nominal CAD geometry after the curing cycle has been completed.

PIDs are the combined effect of spring-in and warpage, which are the two deformation mechanisms that coexist in complex composite structures [1]. Spring-in is defined as the reduction of the angle of a part from a nominal value, while warpage is defined as the change of a part curvature after the manufacturing.

The variety of factors that contribute to PID of composite structures and their relative significance has been studied by various researchers analytically [2,3], experimentally [4–9] and numerically [10–15].

Albert et al. were the first to separate the factors that affect PID into two categories namely intrinsic, which are related to part design (part geometry, material properties etc.) and extrinsic, which are related to tooling or processing (curing cycle, tool part interaction etc.) [1]. An experimental investigation was also carried out by the researchers to understand effect of design and process parameters on spring-in and

warpage of C- and L-shaped composite specimens. They concluded that both design and process parameters can have a significant effect on spring-in and warpage and that there are multiple interactions between them. They also found that using aluminium tooling always results in higher spring-in compared to using steel tooling [1]. Kappel attributed this finding to the difference of the Coefficient of Thermal Expansion (CTE) of the tool and the composite structure when the latter is pressed to the tool due to the autoclave pressure along with geometrical locking if present [16]. Furthermore, Zeng et al. suggest that the shape of the part has significant influence on the warpage [17]. To reduce the stress transfer from the tool to the part, carbon epoxy and carbon foam tools are proposed to be used [18]. The use of sandwich structures instead of monolithic ones is proposed by Al-Dhaheri et al. [19]. It was found that by increasing sandwich core thickness and flexural rigidity the spring-in behaviour declines [20,21] while the CTE and Poisson's ratio of the core were the major contributors to spring-in [22].

Svanberg concluded that the difference in the CTE between the matrix and the fibres, the chemical shrinkage of the resin, the laminate lay-up as well as the CTE of the tool have a large effect on the induced residual stresses in the part [23]. The void content and the fibre content

\* Corresponding author at: The University of Nottingham, Faculty of Engineering, Polymer Composites Research Group, Advanced Manufacturing Building, 522 Derby Rd, Nottingham NG8 1BB, United Kingdom.

E-mail address: [Neoklis.Traiforos@nottingham.ac.uk](mailto:Neoklis.Traiforos@nottingham.ac.uk) (N. Traiforos).

<https://doi.org/10.1016/j.compstruct.2023.116772>

Received 12 September 2022; Received in revised form 23 December 2022; Accepted 3 February 2023

Available online 10 February 2023

0263-8223/© 2023 The Author(s). Published by Elsevier Ltd. This is an open access article under the CC BY license (<http://creativecommons.org/licenses/by/4.0/>).

gradients of the composite have moderate effect. On the contrary, cure time and tool thermal conductivity are reported to have little or no effect at all on shape distortions.

To predict PID of composites analytical [24–26], semi analytical [27] and numerical approaches have been proposed [28–30].

The analytical models are usually used to get a first estimation of the spring-in angle of the structure and for benchmarking new material models [31–33]. Radford proposed a simple analytical formula (Eq. (1)) for the calculation of spring-in angle of angled sections by taking into account the CTE and Chemical Shrinkage Coefficient (CSC) of the structure [34].

$$\Delta\theta = \theta \left[ \frac{(CTE_L - CTE_T)\Delta T}{1 + CTE_T\Delta T} + \frac{CSC_L - CSC_T}{1 + CSC_T} \right] \quad (1)$$

where  $\theta$  is the included angle of the structure,  $\Delta\theta$  is the change in included angle,  $\Delta T$  is the change in temperature,  $CTE_L$ ,  $CSC_L$  and  $CTE_T$ ,  $CSC_T$  are the in-plane and through-thickness CTE and CSC, respectively.

Eq. (1) assumes that the in-plane properties of the laminate are quasi-isotropic and the through-thickness properties are uniform throughout the laminate. Eq. (1) takes into account the effect of stacking sequence on the predicted spring-in angle, however, it does not take into account the effect of specimen thickness, corner radius and extrinsic parameters such as tooling effects. Despite its limitation, Eq. (1) is widely used in the industry and academia, which motivated the use of this formula in this research. In contrast, semi-analytical approaches can take into account the effect of some of these factors (e.g. thickness of the structure), that analytical models cannot, but they require experimentally measured values as input data [35].

In terms of the numerical approaches, elastic, modified elastic and viscoelastic material models have been proposed. The elastic material models make use of the Hooke's law constitutive equation and focus on the development of the PID during the cool down phase of the curing cycle when the structure has attained its final degree of cure, assuming elastic material behaviour at this stage.

The modified elastic models separate the curing history into a number of segments to which they assign an elastic modulus for calculating the residual stresses and distortion of the structure. The Cure Hardening Instantaneously Linear Elastic (CHILE) model divides the curing history into three states: a viscous state, the state where the modulus quickly builds, and the fully cured state where no further chemical reaction takes place [36]. The CHILE model has been used by several researchers [37–39] as well as used to benchmark the development of other material models [40–44]. However, it is still an instantaneously elastic model and cannot predict the stress relaxation during curing or post curing, as it is not a time dependent model [45,46].

In order to incorporate all the time dependent factors that affect shape distortion, such as heating and cooling rates, stress relaxation and cure time, viscoelastic material models are needed [47]. However, implementation of a viscoelastic model in composites with a constitutive update scheme, requires a proper choice of state variables as shown by Poon et al. [48].

In spite of the amount of work performed in this field so far, an accurate estimation of PID in complex geometries remains an open research topic [49–52]. This is mainly due to the great number of factors that contribute to PID, their interdependence and the variability of process conditions and material properties.

The scope of this research is to experimentally investigate the influence of stacking sequence, specimen thickness, tooling material and curing cycle on the spring-in angle of L-shape composite structures. The aim is to identify the driving factors affecting PID and to enrich the literature in this field by studying these parameters on the EPIKOTE™ System 600 resin system with unidirectional (UD) and biaxial Non-Crimp Fabric (NCF) consisting of IMS65 fibres. To the best knowledge of the authors, such an extensive experimental investigation on PID for this material system does not exist in the literature and is presented here for the first time.

The motivation to study alternative to INVAR tooling materials is to reduce manufacturing costs by replacing the INVAR alloy with cheaper tooling materials where possible. Steel tools are already used to produce secondary structures in the aerospace industry but for the majority of the primary structures INVAR tooling is used. By evaluating the effect of tool-part interaction in this material system, the authors wish to facilitate the wider adoption of INVAR alternatives.

Another goal of the research is to further experimentally validate the chemo-mechanical simulation framework for PID developed by the authors and applied for the case of an aerospace composite test frame [53]. This validation enables the extension of the simulation framework to a thermo-chemo-mechanical one, with the addition of a heat transfer analysis prior to the mechanical analysis for the material system under investigation. With the motivation to further increase the accuracy of the simulation framework, tool-part interaction is also included in the simulation by employing a constant and cure dependent coefficient of friction. This extended simulation framework is also presented here for the first time and applied to predict the spring-in angle of the composite L-shape specimens.

A comparison between simulation results using a modified CHILE and viscoelastic material models, Eq. (1) and the experimentally measured spring-in angle of the specimens is presented. The aim is to identify a combination of the material model and boundary conditions which more efficiently predicts the shape of the manufactured part in terms of accuracy and modelling effort.

## 2. Experimental procedure

The L-shape composite structure that was studied in this research is depicted in Fig. 1. The nominal included angle between the flanges of the specimens is 90°, the corner radius is 15 mm, the length of each flange is 100 mm and the width of the specimens is 50 mm. Three tools were manufactured from INVAR, steel and aluminium alloy as depicted in Fig. 2, to investigate the effect of the CTE of the tool material on the PID of the specimens. To manufacture the tools, 6 mm thick plates were laser cut, bent and welded to their nominal dimensions. The included angle of the tools manufactured, was measured using a Coordinate Measurement Machine (CMM) and found to be 90.24°, 89.68° and 89.37° for the INVAR, steel and aluminium tool, respectively. The properties of the tooling materials are presented in Table 1.

Composite specimens were manufactured by vacuum assisted infusion method (Fig. 3) using EPIKOTE™ System 600 resin system supplied by Hexion [54]. A unidirectional (UD) and a biaxial (+45°/−45°) non-crimp fabric (NCF), manufactured by Teijin Carbon, were used for creating preforms. The areal weight of UD and biaxial NCF was 194 g/m<sup>2</sup> and 407 g/m<sup>2</sup>, respectively, including toughening veil (5 g/m<sup>2</sup>) and powder binder (7 g/m<sup>2</sup>). Both of the reinforcements consisted of IMS65 fibres supplied by Toho Tenax. The properties of the IMS65 fibre were found in literature [55] or, where not explicitly defined by the supplier, were assumed to be equal to the properties of AS4 fibre [36]. The fibre properties used in this research are presented in Table 2.

The stacking sequences of the specimens manufactured are given in Table 3 along with their abbreviation. Underscores in the stacking sequence denote the use of NCF. Bending stiff (BS) and bending compliant (BC) laminates were chosen to be manufactured in addition to representative skin (SK), frame (FR), stiffener (ST) and spar (SP) laminates to examine the effect of laminate bending stiffness on spring-in angle. Antisymmetric (AS) and heavily unbalanced (UB) laminates were also manufactured to examine the applicability of the developed materials models for these extreme cases. To increase the difference of the bending stiffness of the specimens, 8, 16 and 24 plies specimens were manufactured. The subscripts of the laminate notations refer to the equivalent total number of plies of each design.

Three specimens of each laminate design were manufactured using the INVAR tool. Also, three specimens of the  $BS_{16}$ ,  $SP_{16}$  and  $ST_{16}$  laminate designs were manufactured using each of the aluminium and

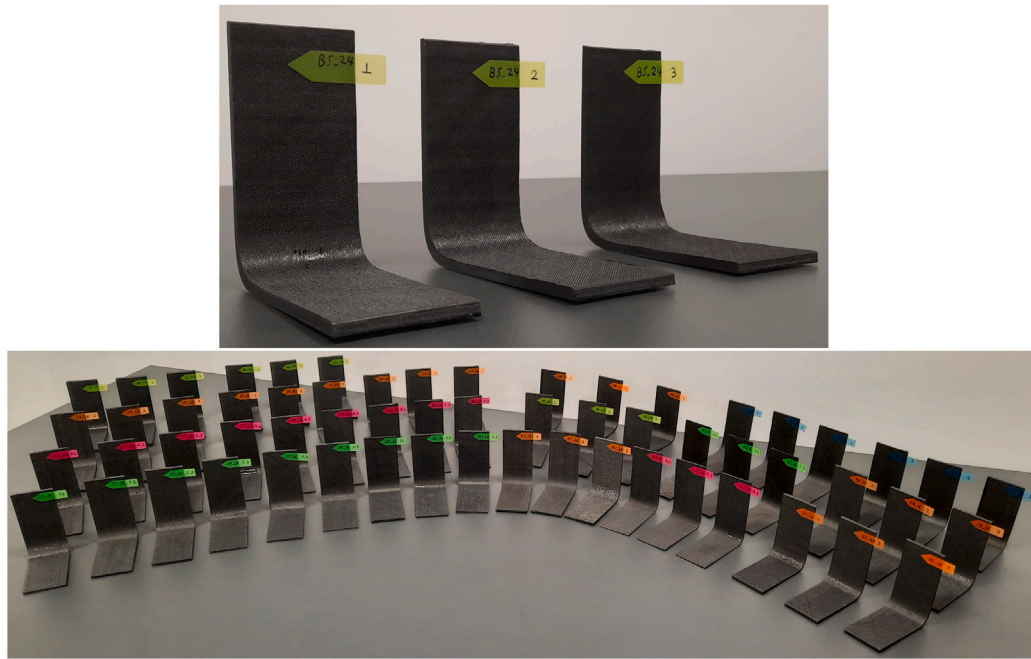


Fig. 1. The L-shape composite specimens of the Bending Stiff 24 plies ( $BS_{24}$ ) laminate group studied (top). All the specimens manufactured (bottom).



Fig. 2. The three tools used to manufacture the specimens (From top to bottom: Steel, Aluminium and INVAR).

Table 1  
Material properties of the tools manufactured.

Physical property	INVAR	Steel	Aluminium
CTE ( $K^{-1}$ )	6 E-07	1.2 E-05	2.34 E-05
E-Modulus (GPa)	140	207	70
Poisson coef.	0.29	0.30	0.35

steel tools. To manufacture the preforms, rectangular plies with a length of 220 mm and width 70 mm were stamped in a press from the fabric rolls with the use of a custom die. Two specimens were usually placed side by side on a tool as shown in Fig. 3 and where possible, placed in the oven with other tools that were to be subjected to the same curing cycle. One peel ply fabric layer was used per moulding on top of which the resin flow mesh was placed. The peel ply fabric layer and the resin flow mesh had the same dimensions per bagging set-up. Furthermore, the location of the resin injection and outlet hose was approximately the same for every moulding.

Table 2  
Material properties of the IMS65 carbon fibre.

Physical property	Symbol	Value	Units	Source
CTE	$CTE_{11}$	-1.00 E-07	[1/°C]	Approximated
	$CTE_{22}$	4.83 E-06	[1/°C]	Approximated
Modulus	$E_{11}$	290	[GPa]	Toho Tenax [55]
	$E_{22}$	17.24	[GPa]	AS4 fibre [36]
	$G_{12}$	27.60	[GPa]	AS4 fibre [36]
Poisson coef.	$\nu_{12}$	0.20	-	AS4 fibre [36]
	$\nu_{23}$	0.25	-	AS4 fibre [36]
Density	$\rho_f$	1780	[kg/m <sup>3</sup> ]	Toho Tenax [55]

Table 3  
The stacking sequences of the specimens manufactured.

Laminate	Stacking sequence	0 (%)	±45 (%)	90 (%)	t (mm)
$BS_8$	$[0/90_2, 45/-45]_s$	25	50	25	1.62±0.06
$BC_8$	$[45/-45, 90/0]_s$	25	50	25	1.60±0.05
$BS_{16}$	$[0/90_2, 45/-45]_s$	25	50	25	3.08±0.08
$BC_{16}$	$[45/-45, 90/0]_s$	25	50	25	3.07±0.09
$SK_{16}$	$[45/-45, 0/90, 0_2]_s$	38	50	13	3.04±0.07
$FR_{16}$	$[45/-45, 0, 45/-45, 0/90, 45]_s$	25	63	13	3.09±0.08
$ST_{16}$	$[45/-45, 0/90, 0_4]_s$	63	25	13	3.04±0.08
$SP_{16}$	$[45/-45, 90/0]_s$	13	75	13	3.06±0.08
$AS_{16}$	$[0/90_2, 45/-45, 0/90_2]_s$	25	50	25	3.12±0.11
$UB_{16}$	$[0/90_2, 45_4]_s$	25	50	25	3.05±0.08
$BS_{24}$	$[0/90_3, 45/-45]_s$	25	50	25	4.62±0.09
$BC_{24}$	$[45/-45, 90/0]_s$	25	50	25	4.56±0.10

The specimens were manufactured using the Manufacturer Recommended Curing Cycle (MRCC) depicted in Fig. 7 [54]. Four thermocouples were used for monitoring the temperature during the cure cycle as shown in Fig. 4. Two thermocouples were placed on the underside of the tool at each flange near the tool corner, one in the bag and another one on top of the vacuum bag at the L-shape corner to measure the air temperature at this location.

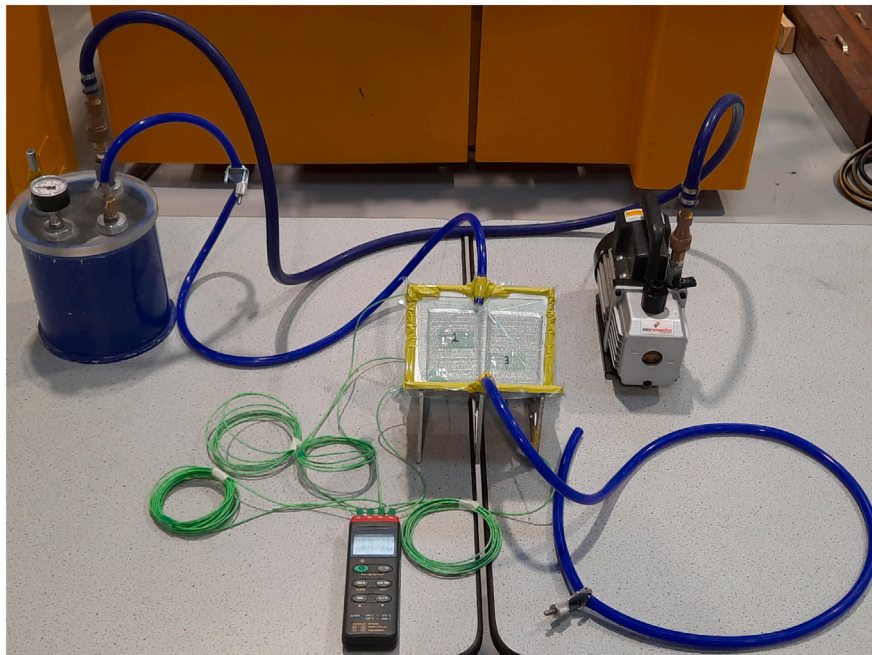


Fig. 3. Two specimens side by side under vacuum, prior to the resin infusion process. The tool enters the oven where it is preheated at 120 °C while the resin is simultaneously preheated at 80 °C in a separate oven. When the respective temperatures have been reached the infusion takes place through the inlet tube (right) which enters the oven to the tool and the outlet tube which exits the oven to the catch-pot (left).

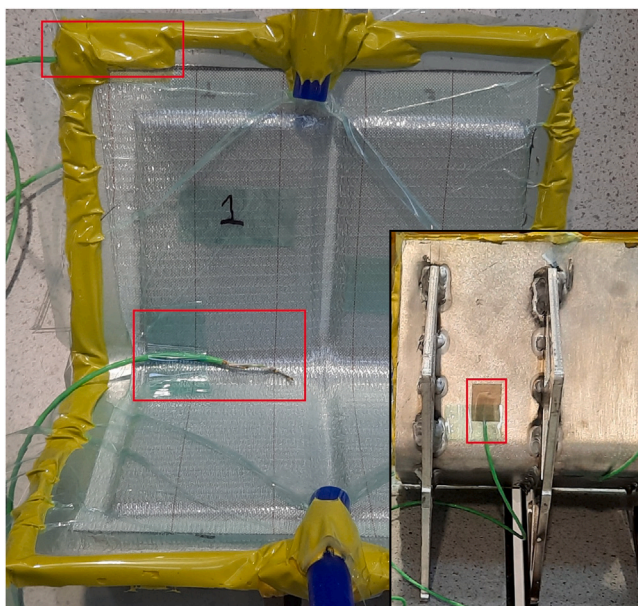


Fig. 4. Thermocouple setup: Two thermocouples were placed on the underside of the tool near the corner (bottom right, one in each flange), one thermocouple was placed in the bag under the sealant tape (top left) and another one was placed on top of the vacuum bag at the L-shape corner to measure air temperature at this location.

Prior to resin infusion, the assembly was preheated to 120 °C in an oven. The resin was preheated in a separate oven to 80 °C in order to achieve the manufacturer’s recommended resin viscosity of approximately 280 mPa·s [54]. When the assembly in the oven reaches 120 °C, the resin infusion starts, and the resin’s viscosity drops as it enters the preform. During the infusion, a slight drop of the assembly temperature is recorded by the thermocouple as depicted in Fig. 7 because the resin is cooler than the tool and preform. After the infusion

is finished and the assembly temperature again reaches 120 °C, a heat-up phase follows to the curing temperature of 180 °C, where the specimen is cured for two hours. When the curing process is over, the oven is switched off and the assembly is left in the oven to cool down to the room temperature. The heating and cool down rates are kept below 2.5 °C/min to avoid the development of significant temperature gradients through the thickness of the parts.

In order to evaluate the effect of the curing cycle on PID of the parts, the  $BS_8$  and  $BC_8$  laminate designs were also manufactured by another curing cycle denoted hereafter as the “Fast” curing cycle. This curing cycle differs from the MRCC as the two hours of 180 °C dwell was substituted by a 15 min 195 °C dwell. The “Fast” curing cycle was designed to produce approximately the same final degree of cure as the MRCC.

After the curing process was finished the specimens were demoulded and visually inspected for manufacturing defects (dry spots, delamination, fibre bridging etc.). Specimens with no visible defects were then machined to their nominal dimensions by cutting approximately 10 mm from each side with the use of a diamond wheel saw.

After machining, the thickness of the manufactured specimens was measured with a digital vernier caliper at 18 locations across the flanges of each part and the average value of the measurements along with the standard deviation of each laminate design is presented in Table 3. The nominal thickness of the 8, 16 and 24 ply specimens are 1.47 mm, 2.94 mm, and 4.42 mm, respectively, resulting from the nominal thickness of the UD and biaxial NCF which is 0.184 mm and 0.368 mm respectively.

The geometry of the 16 and 24 plies specimens was measured with the use of a CMM as depicted in Fig. 5. The outer surfaces of the flanges were approximated with the use of 10 × 10 points for each surface, equally spaced across the area of the flange. The measured points on a flange surface were used to fit a plane, by employing a Gaussian best fit algorithm, that represents the actual flange surface. Finally, the included angle of the specimen was determined as the angle between the normal vectors of the two fitted planes. The plane fitting and measurement of the angles of the specimens was done with the use of the GOM Inspect suite [56]. The geometry of 8 plies specimens

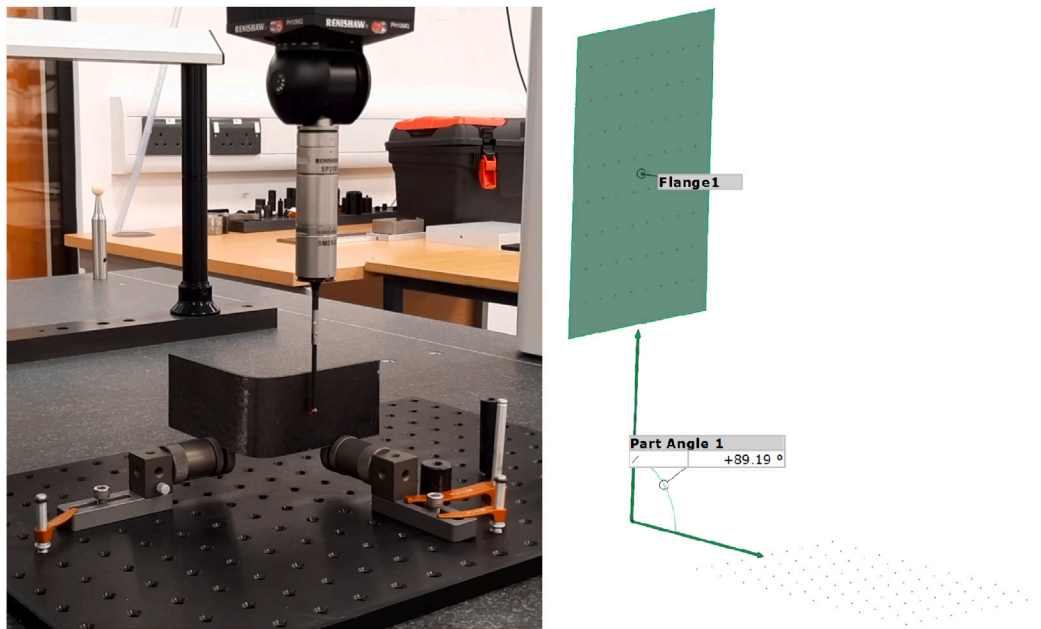


Fig. 5. Measurement of process induced distortions of the  $BC_{16}$  specimen 1 in the Coordinate Measuring Machine (left). Plane fit and calculation of spring-in angle (right).

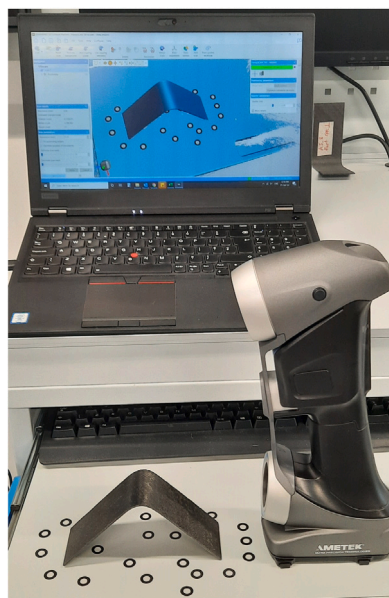


Fig. 6. Measurement of process induced distortions of the  $BS_8$  specimen 2 with the Creaform 3D HandySCAN.

was scanned with the use of Creaform 3D HandySCAN instead of the CMM as shown in Fig. 6. This was done because of the low bending stiffness of the 8 plies specimens and the measurement error that the fixture of the CMM may induce to the measurement of these parts. The cloud of points obtained by the 3D scanner was used to follow the same post-processing procedure as described above.

### 3. Material modelling

The material modelling effort focuses mainly on the evolution of the resin properties during cure, since fibre properties change insignificantly during the manufacturing process. Depending on the thickness

of the structure a chemo-mechanical or a sequentially coupled thermo-chemo-mechanical analysis was implemented to model the change of the material properties during the manufacturing process.

According to the work of Chen [28], a thickness threshold of 3 mm was chosen after which a heat transfer analysis should be employed prior to the spring-in analysis in order to identify temperature gradients in the part that lead to significant property gradients affecting its distortion. Parts with a thickness of less than 3 mm are considered to have a homogeneous temperature field, an assumption made to reduce computational cost.

The chemo-mechanical and thermo-chemical modules presented thereafter can be used independently or can be coupled. Where a sequentially coupled thermo-chemo-mechanical analysis is needed the thermal analysis runs first and the temperature field at every time step is mapped to the spring-in analysis as depicted in Fig. 8.

#### 3.1. Thermo-chemical module

The scope of the thermo-chemical module developed is to calculate the temperature field in the part at every time step. First, the resin conductivity and specific heat capacity are calculated as a function of temperature and degree of cure. The thermal properties of the fibre are calculated as a function of temperature only. The instantaneous fibre volume fraction is also calculated based on the resin chemical contraction and thermal expansion as depicted in Fig. 9.

Then, the effective thermal properties of the lamina can be calculated with the use of the instantaneous thermal properties of the resin and fibres, along with the resin exothermic heat reaction. Finally, this information is given as input to the thermal constitutive equation to calculate the temperature distribution of the time increment in the part as shown in Fig. 9.

#### 3.2. Chemo-mechanical module

The chemo-mechanical simulation module used in this work was developed and presented in detail by the authors in [53]. The module updates the stress tensor and Consistent Tangent Operator (CTO) at the material integration points at every time increment of the curing history. As shown in Fig. 10, the resin properties depend on the degree of cure and temperature of the time increment.

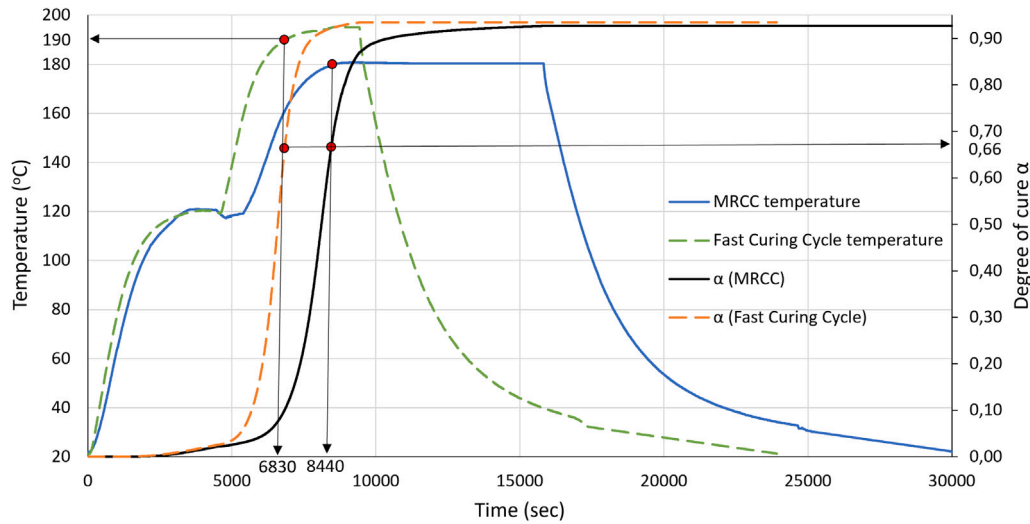


Fig. 7. The two curing cycles investigated: According to the Manufacturer Recommended Curing Cycle (blue curve) the part cures for 2 h at 180 °C. The Fast curing cycle investigated (green curve) achieves the same result in terms of final degree of cure with a 15 min dwell at 195 °C. The evolution of the degree of cure of the two curing cycles is a s-type curve and the red dots depict the gelation of the structure, which is the starting point of the spring-in simulation framework developed. The resin is infused in the preform at 120 °C where a slight drop of the laminate temperature is observed. The temperature data of the curing cycles presented was obtained from the thermocouple placed in the vacuum bag.

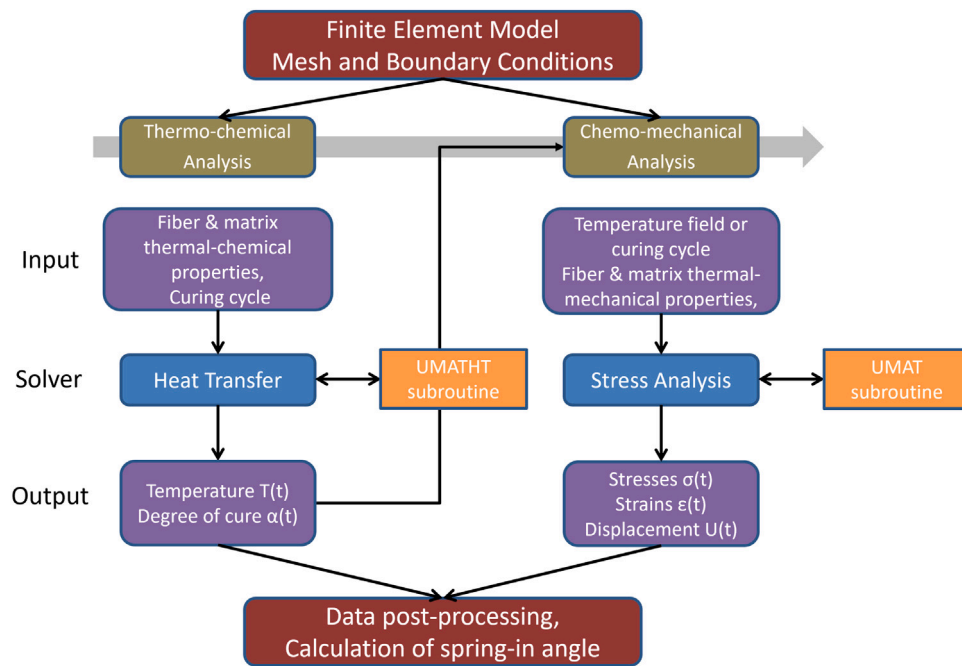


Fig. 8. Interaction between the thermal–chemical and mechanical modules. Blue colour indicates variable calculation, purple access of memory, orange call of the subroutines developed and red use of pre and post processing software.

The first step in the calculation process is to calculate the degree of cure at the current time increment. Then the resin material properties such as the instantaneous glass transition temperature  $T_g$ ,  $E$  and  $G$  moduli and Poisson coefficient  $\nu_r$ , can be calculated. The instantaneous thermal and chemical strains and fibre volume fraction coefficient are calculated prior to the calculation of the effective material point's properties (homogenization step). The homogenization step refers to the use of a micromechanics model to calculate the effective modulus and expansion coefficients of the material point usually by assuming orthotropic or transversely orthotropic material behaviour [53].

Following the homogenization step, the stiffness matrices can be assembled along with the calculation of the strains at the material

points. Finally, this information is supplied as input to the constitutive equation of the material model employed, in order to update the stress tensor and CTO of the time increment for the next iteration to proceed. All material model and constitutive equations used by the chemo-mechanical module and those jointly used by the thermo-chemical module (cure kinetic model, glass transition temperature, resin CTE etc.) are not presented here and can be found in [53].

### 3.3. Cure and temperature dependent material properties

#### 3.3.1. Resin conductivity

The resin conductivity,  $k_r$ , was approximated as a weighted sum of the fraction of the values of the liquid and fully cured state as given

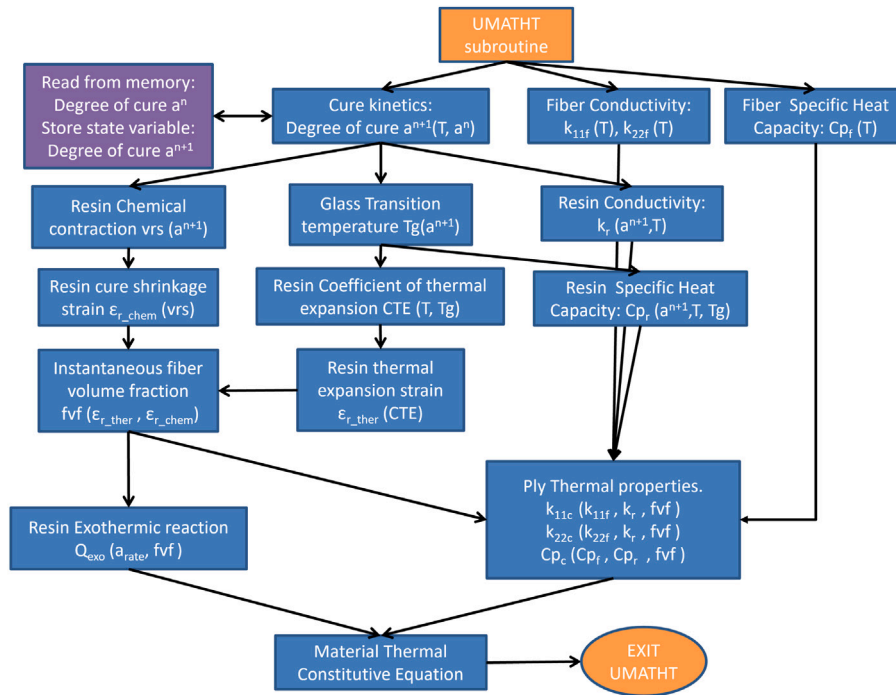


Fig. 9. Thermo-chemical module. Blue colour indicates variable calculation, purple access of memory, orange start/finish of the calculation process.

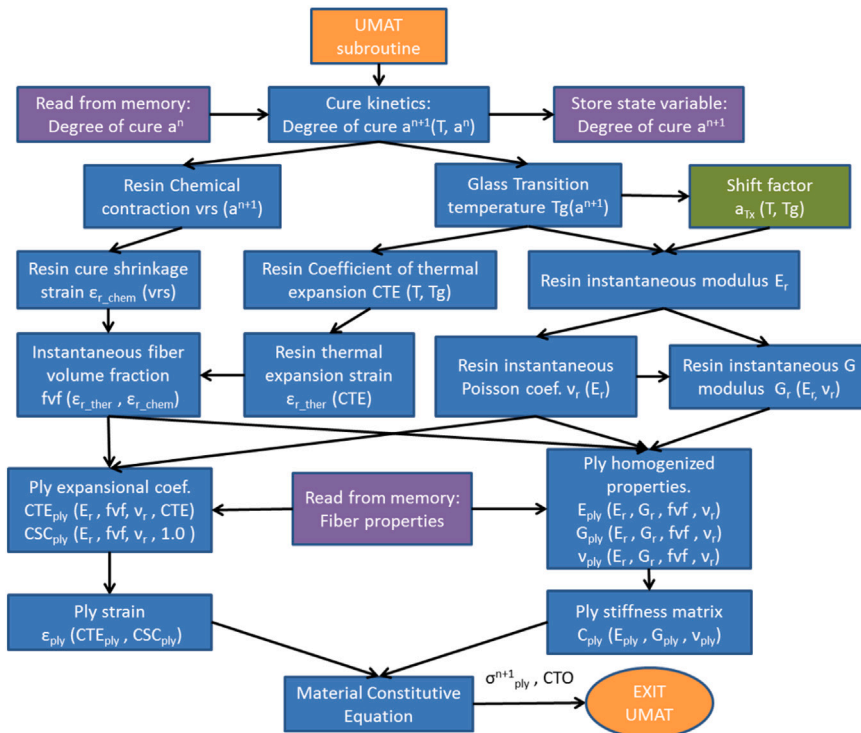


Fig. 10. Chemo-mechanical module. Blue colour indicates variable calculation, purple access of memory, orange start/finish of the calculation process. The calculation of the combined shift factor  $a_{Tx}$  (green box) is employed only by the viscoelastic material model [53].

in Eq. (2). In the absence of specific material data of the resin under investigation, the material constants of the EPON 862/EPIKURE 3300 epoxy system are used [28].

$$k_r = 0.148(1 - \alpha) + k_{r1} \alpha \quad (2)$$

where  $k_{r1}$  is the conductivity of the fully cured resin defined as:

$$k_{r1} = 6.097 * 10^{-4} T + 0.0236 \quad (3)$$

In Eq. (2),(3)  $\alpha$  is the degree of cure and  $T$  is the temperature of the increment.

**Table 4**

Degrees of freedom constrained per boundary condition type. The nodes numbering refer to Fig. 11.

BC type	Nodes	DOFs constrained
Freestanding	Node 1	x
	Node 2	x, y
	Node 3	x, y, z
Fixed	All FE nodes	x, y, z

### 3.3.2. Resin specific heat capacity

The specific heat capacity of the resin was determined with DSC and was approximated according to Eq. (4) and (5) [57,58]:

$$c_{p_r} = c_{p_{rub}} + \frac{c_{p_g} - c_{p_{rub}}}{1 + e^{k_{fac}(T^* - D_{TC})}} \quad (4)$$

where

$$\begin{aligned} c_{p_g} &= (1 - \alpha)c_{p_{g_0}} + \alpha c_{p_{g_\infty}} \\ c_{p_{g_0}} &= s_{g_0}T + c_{g_0} \\ c_{p_{g_\infty}} &= s_{g_\infty}T + c_{g_\infty} \\ c_{p_{rub}} &= (1 - \alpha)c_{p_{r_0}} + \alpha c_{p_{r_\infty}} \\ c_{p_{r_0}} &= s_{r_0}T + c_{r_0} \\ c_{p_{r_\infty}} &= s_{r_\infty}T + c_{r_\infty} \end{aligned} \quad (5)$$

where  $s_{r_0}, s_{r_\infty}, s_{g_0}, s_{g_\infty}, c_{r_0}, c_{r_\infty}, c_{g_0}, c_{g_\infty}, k_{fac}, D_{TC}$  are material constants, and  $T^* = T - T_g$ , where  $T_g$  is the glass transition temperature of the time increment [53].

### 3.3.3. Fibre conductivity

The conductivity of the fibre (Eq. (6)) is a function of temperature and was assumed to be the same as that of AS4 fibre [36]:

$$\begin{aligned} k_{11_f} &= 7.7 + 1.56 * 10^{-2}T \\ k_{22_f} &= 2.4 + 5.07 * 10^{-3}T \end{aligned} \quad (6)$$

### 3.3.4. Fibre specific heat capacity

The specific heat capacity of the fibre is a function of temperature (Eq. (7)) and was assumed to be the same as that of AS4 fibre [36].

$$c_{p_f} = 750 + 2.05T \quad (7)$$

### 3.4. Thermal micromechanics model

After the calculation of the instantaneous properties of the resin and the fibre the next step in the material modelling process is to calculate the effective lamina thermal properties by employing micromechanics models.

- Resin instantaneous density

The resin instantaneous density is calculated according to Eq. (8) based on the resin's specific volume change due to thermal and chemical strains:

$$\rho_r^0 = \frac{\rho_r^0}{1.0 + V_r^T - V_r^C} \quad (8)$$

where  $\rho_r^0 = 1.15 \text{ g/cm}^3$  is the resin density at 25 °C and  $\alpha = 0$  [54].  $V_r^T$  and  $V_r^C$  are the resin specific volume change due to thermal and chemical strain respectively [53].

- Lamina density

The density of the lamina is calculated using the rule of mixtures (Eq. (9)) [36]:

$$\rho_c = \rho_f V_f^0 + \rho_r^0 (1 - V_f^0) \quad (9)$$

where  $V_f^0$  is the instantaneous fibre volume fraction [53].

- Lamina effective specific heat capacity

The effective specific heat capacity of the lamina is calculated according to (Eq. (10)) [36]:

$$c_{p_c} = \frac{c_{p_f} \rho_f V_f^0 + c_{p_r} \rho_r^0 (1 - V_f^0)}{\rho_c} \quad (10)$$

- Lamina effective conductivity

The lamina longitudinal conductivity  $k_{11_c}$  is determined using the rule of mixtures. The transverse conductivity  $k_{22_c}$  is calculated according to the Extended Concentric Cylinder Assemblage (ECCA) model (Eq. (11)) [28]:

$$\begin{aligned} k_{11_c} &= k_{11_f} V_f^0 + k_r (1 - V_f^0) \\ k_{22_c} &= \frac{(1 + V_f^0)k_{22_f} + (1 - V_f^0)k_r}{(1 - V_f^0)k_{22_f} + (1 + V_f^0)k_r} k_r \end{aligned} \quad (11)$$

### 3.5. Thermal constitutive equation

The Fourier's law constitutive equation (Eq. (12)) is the governing equation for the heat transfer model:

$$\rho_c c_{p_c} \frac{\partial T}{\partial t} = \nabla \cdot (k_c \cdot \nabla T) + \dot{Q} \quad (12)$$

where  $k_c$  is the conductivity tensor of the composite and  $\dot{Q}$  is the exothermic heat reaction of the resin (Eq. (13))

$$\dot{Q} = \rho_r^0 (1 - V_f^0) H_r \dot{\alpha} \quad (13)$$

In Eq. (13),  $H_r$  is the resin heat of reaction and  $\dot{\alpha}$  is the curing rate [53].

### 3.6. Boundary conditions

#### 3.6.1. Mechanical boundary conditions

Regarding mechanical boundary conditions, freestanding and fixed boundary conditions were investigated. A more physically representative tool-part interaction approach was also employed to assess its ability to accurately predict the deformed shape of the part. Freestanding boundary condition implies that three nodes are used to suppress rigid body motion of the part during all simulation steps as shown in Fig. 11 and Table 4. On the other hand, the fixed mechanical boundary condition implies that all the translational Degrees of Freedom (DOFs) of all nodes of the mesh are set to zero displacement until the cool down step is over. Then, a demoulding step is added to the simulation in which the fixed mechanical boundary condition is deactivated and three nodes as shown in Fig. 11 are used to suppress rigid body motion of the part. At this step the internal stresses of the part are released and the part deforms.

The effect of tool-part interaction was also evaluated by modelling the tool and using Coulomb's friction approach to model the stick/slip behaviour and transfer of shear forces at the interfaces. For the tangential directions an isotropic Coefficient of Friction (CoF) was used with a shear stress limit of  $\tau_{max} = 0.14 \text{ MPa}$  after which sliding of the interfaces occurs [5]. Both fixed and cure-dependent CoF in the tangential direction were examined. A typical value for the fixed CoF for modelling the tool-part interaction is  $\mu_{fixed} = 0.3$  [5,14].

However, the CoF during the curing process is not constant but depends on the state of material during the curing cycle [17]. To accurately model the evolution of the CoF during the cure, an experimental investigation such as those presented in [59–61] should be performed prior to the tool-part interaction modelling to determine the shear stress limit after which sliding occurs. Also, an analytical formula can be experimentally determined, which describes the evolution of CoF of the material system as a function of temperature or degree of cure of the curing cycle. This is a time consuming and costly process and usually this approach is not followed. Therefore here, the linear function Eq. (14) derived from the work of Zeng [17] is adopted,



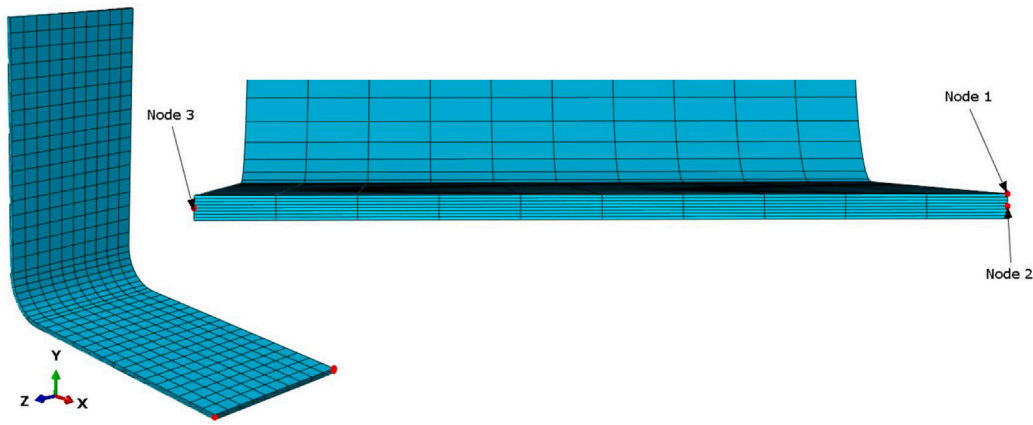


Fig. 11. The three nodes used to suppress rigid body motion of an 8-ply specimen at the freestanding boundary condition.

to describe the evolution of the CoF,  $\mu(\alpha)$ , from the gelation of the structure to cool down. The degree of cure was calculated at every time step of the simulation and was used as input to the contact algorithm in the form of User Defined Field in ABAQUS.

$$\mu(\alpha) = 1.05\alpha - 0.53 \quad (14)$$

A hard contact was employed in the normal direction of the tool-part interfaces to prevent the parts penetrating each other. At the faces of the composite part in contact with the vacuum bag a pressure field was applied equal to atmospheric pressure. Finally, three nodes are used to suppress rigid body motion of the tool during the curing cycle, similar to those shown in Fig. 11 for the composite part.

### 3.6.2. Thermal boundary conditions

The tool and the composite part inside the oven are both heated or cooled through convection of the air. The convective boundary condition can be formulated as:

$$(k_c \cdot \nabla T) \cdot \vec{n} = h(T_s - T_\infty) \quad (15)$$

where  $\vec{n}$  is the unit vector normal to the surface,  $h$  is the heat transfer coefficient,  $T_s$  is the surface temperature of the part and  $T_\infty$  is the oven air temperature.

The heat transfer coefficient  $h$  in the oven is a function of oven free stream temperature, air pressure and velocity, turbulence of air, positioning and orientation of the assembly in the oven [17,36]. To determine the heat transfer coefficient  $h$  in the oven Computational Fluid Dynamics (CFD) simulation, empirical models or measurements are typically performed [17].

In the thermo-chemical analysis employed in this study a heat transfer coefficient was used to simulate the heat flow from the vacuum bag to the composite part at the faces of the part in contact with the bagging set-up (peel ply, resin flow mesh, vacuum bag) and another one to simulate the heat flow to the composite part from the tool surface. To avoid costly CFD simulations or indirect measurements of the heat transfer coefficients, the values used in the simulations were approximated. As input to the simulations, values of the heat transfer coefficients as measured by Premium AEROTEC GmbH in one of their ovens, for manufacturing U-shaped composite aerospace frames on an INVAR tool were used. The bagging materials (vacuum bag, resin flow mesh, peel ply fabric) used in this study are similar to the bagging set up of the measurement. Even though identical conditions cannot be replicated as the oven and geometry of tools differ, it was assumed in this study that  $h_{bag} = 8 \frac{W}{m^2K}$  represents the heat flow from the bag to the composite part and  $h_{mould} = 17 \frac{W}{m^2K}$  the heat flow from the tool to the part. The oven air temperature  $T_\infty$  is set equal to the temperature recorded by the thermocouple placed on top of the vacuum bag.

## 4. Numerical implementation

The material modelling presented in Section 3 was implemented in ABAQUS with the use of customized User Material Subroutines (UMAT and UMATHT).

In the case of the 8 and 16 ply specimens a chemo-mechanical simulation approach was implemented to calculate the distortion of the parts, since the thickness of the specimens is less than or close to 3 mm (Table 3). Consequently, the temperature used as input in these simulations is assumed to be homogeneous and identical to the temperature measured by the thermocouple placed in the bag (Fig. 7). Even though this assumption is not strictly valid, the slow heating and cooling rates suggested by the MRCC contribute to a nearly homogeneous temperature field across the part.

The starting point of the chemo-mechanical simulation is the gelation of the resin as depicted with the red dot in Fig. 7. Stresses built up earlier in the curing cycle are assumed to contribute insignificantly to the process induced distortion of the specimens. The curing history was divided into three steps from the gelation of the resin, one to simulate the heating step to the curing temperature, another step of the isothermal hold of the structure at 180 °C and a third one for the cool down of the structure to room temperature.

In the case of the 24 ply specimens, a thermo-chemo-mechanical simulation approach was considered as the thickness of the parts is above 3 mm (Table 3) in order to identify temperature gradients in the part that lead to significant property gradients affecting its distortion. The thermo-chemical analysis depicted in Fig. 9 run first and the resulting temperature field was mapped at each time step to the mechanical analysis for the calculation of the distortion of the structure as depicted in Fig. 8.

Finally, to simulate the machining operations after demoulding the Model Change functionality of ABAQUS was used in a separate simulation step. In this step a number of elements were subtracted from the mesh of the L-shape specimen representing the area of the specimen which is going to be trimmed (10 mm from each side of the part).

After the FEA analysis is run the deformed mesh of the part is imported into the GOM Inspect suite. Then, the same process as the one followed for the calculation of the spring-in angle of the manufactured specimens was followed i.e. Gaussian best fit of planes to the flanges of the part and calculation of the spring-in angle based on the angle that the normal vectors of the two planes create.

### 4.1. Meshing

Fig. 12 shows the finite element mesh for the 8 plies, 16 plies tool-part interaction and 24 plies specimens that was used to simulate the process induced distortion of the L-shape structures. The mesh in the

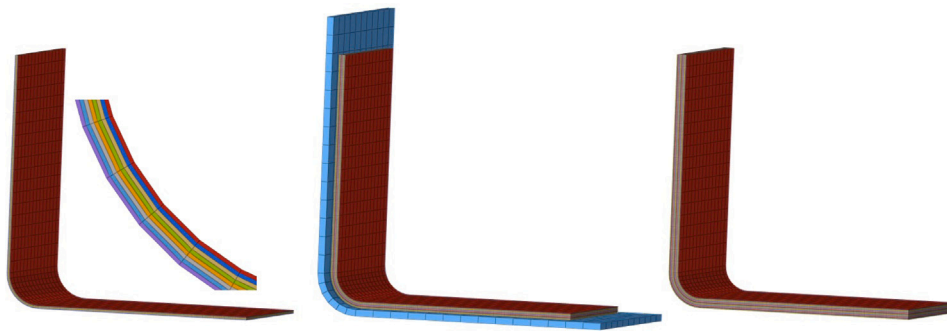


Fig. 12. The finite element mesh used to model the L-shape structures. Each composite ply is modelled with one element in its thickness direction. From left to right, the 8 plies, 16 plies tool-part interaction and 24 plies mesh.

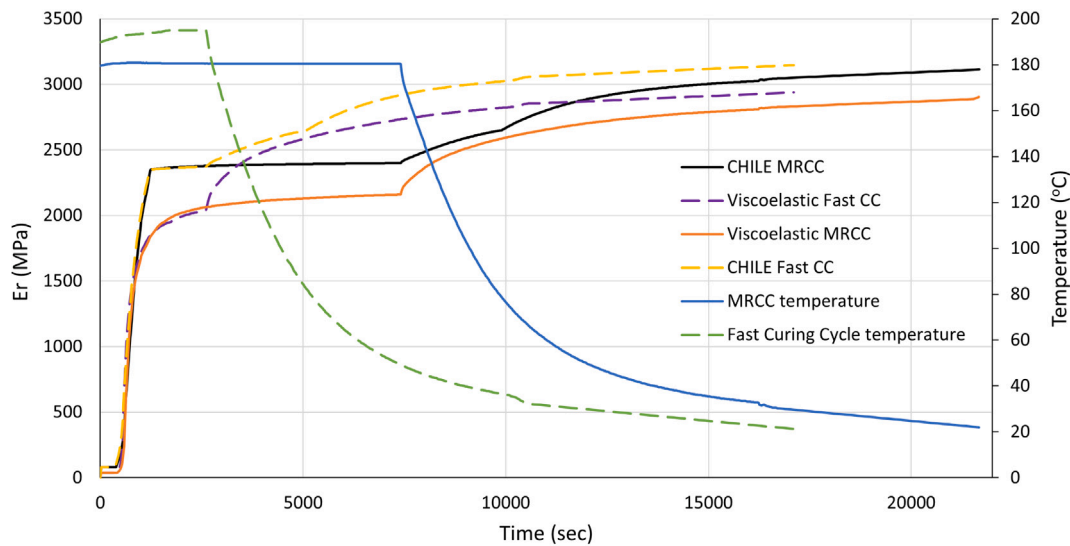


Fig. 13. The Young's modulus development of the resin from the gelation to demoulding the structure, according to the CHILE and the viscoelastic material characterisation for the MRCC and Fast curing cycle.

chemo-mechanical analysis consists of C3D8I solid elements, which have incompatible modes to improve their bending behaviour [62]. Each ply is modelled with the use of one element in the thickness direction with the use of three integration points. An element length of approximately 5 mm was chosen in the longitudinal and transverse direction. The corner of the L-shaped structure was discretised using half the element length in the longitudinal direction as the one used for the flanges (2.5 mm). The angle of the L-shape parts simulated was exactly 90°.

The biaxial NCF was modelled as two UD plies at the respective orientations by ignoring the stitching of the fabric. Consequently, the total number of integration points of a specimen consisting of UD and NCF in the thickness direction is equal to the number of the resulting plies multiplied by three.

The number of elements used for the 8, 16 and 24 plies specimens is 5264, 10,304 and 15,792, respectively. In the tool-part interaction simulation, the tool was modelled with fewer elements compare to the L-shape specimen as shown in Fig. 12.

The mesh in the thermal analysis consists of DC3D8 elements which is an 8-node linear heat transfer brick element. Each ply is modelled with the use of one element in the thickness direction and the element size was equal to the one selected for the chemo-mechanical analysis in order to facilitate the mapping process of the temperature field to the spring-in analysis. To account for the ply orientation, the orientation of the elements belonging to a ply was modified accordingly.

### 5. Results and discussion

The evolution of the degree of cure  $\alpha$  of the resin for the MRCC and “Fast” curing cycles is presented in Fig. 7. It can be seen that the gelation of the structure is reached earlier compared to the MRCC and the final degree of cure is approximately the same for the two curing cycles and equal to  $\alpha_{MRCC} = 0.926$  and  $\alpha_{Fast} = 0.934$ , respectively.

Fig. 13 shows the evolution of the Young's modulus of the resin, according to the CHILE and the viscoelastic material characterisation for the two curing cycles investigated. The “Fast” curing cycle produces a part with higher modulus compare to the MRCC which can be attributed to the slightly higher final degree of cure that the part attains and the earlier gelation of the structure as depicted in Fig. 7. Furthermore, the instantaneous modulus predicted by the viscoelastic model is lower compared to the CHILE model for both curing cycles investigated which is due to different modelling approaches used. In the case of the CHILE model a modified CHILE equation was fitted to DMA data whereas in the linear viscoelastic model a number of Maxwell elements were fitted to DMA data [53].

Fig. 15,16,17 and Fig. 18 depict a comparison between experimental results (specimen 1,2 and 3) and the predicted spring-in angle with use of Eq. (1) and the modified CHILE and viscoelastic material model in relation to the three boundary conditions investigated (freestanding, fixed and tool-part interaction). The tables in Appendix contain the data presented in the figures and the average spring-in angle of the specimens measured with its standard deviation. The results refer to the spring-in angle of the specimens in degrees after demoulding.

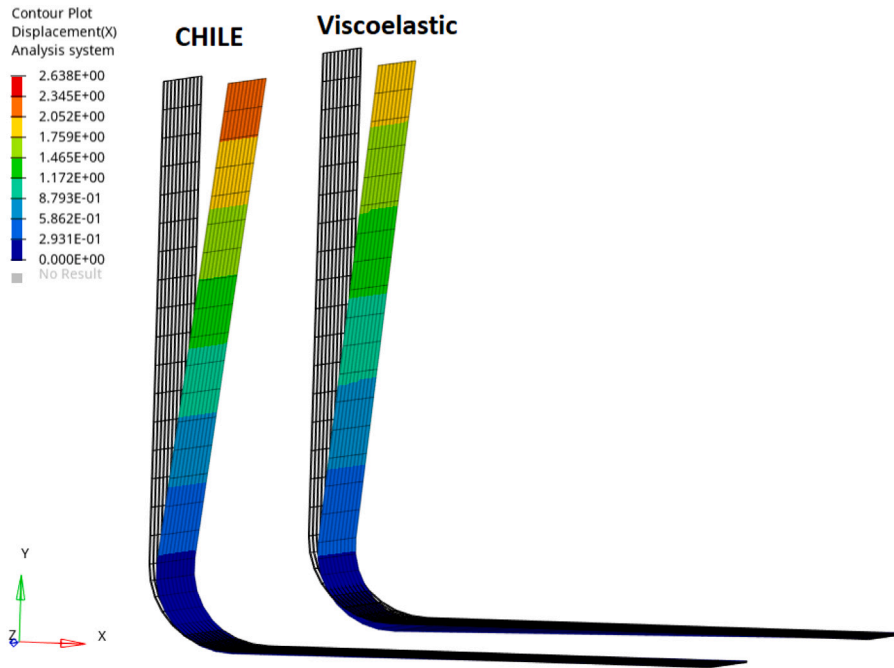


Fig. 14. Distortion field of the first ply of the  $BS_{16}$  group along the  $x$ -axis in mm as predicted by the CHILE (left) and viscoelastic (right) model with the use of the freestanding BC after the trimming step. The distortion field is multiplied by a factor of five and the undeformed shape of the part is shown with the black mesh lines.

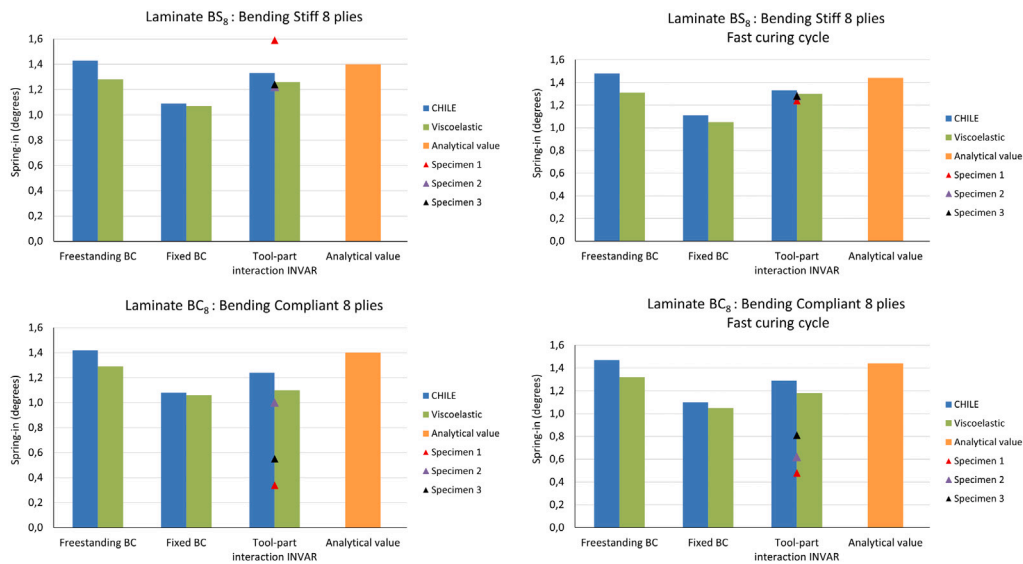


Fig. 15. Experimentally measured (specimen 1–3) and predicted spring-in angle of the 8 plies specimens manufactured.

The 8 plies specimens (Fig. 15 and Table A.1) were manufactured with the MRCC and “Fast” curing cycle from the INVAR tool and were measured with the 3D scanner. All 16 plies parts (Fig. 16 and Table A.2) were manufactured with the INVAR tool and MRCC. The parts presented in Fig. 17 and Table A.3 were also manufactured from the steel and aluminium tools. Finally, the 24 plies specimens (Fig. 18 and Table A.4) were manufactured with the INVAR tool and MRCC. All 16 and 24 ply specimens were measured with the CMM.

The distortion field of the first ply (from the tool side) of the  $BS_{16}$  laminate design along the  $x$ -axis after the trimming step, as predicted by the modified CHILE and viscoelastic model with the use of the freestanding BC is depicted in Fig. 14. The distortion field is scaled by a factor of five in order for the distortions to be visible. The undeformed shape of the part is shown with the black mesh lines in the background. The distortion field for this laminate group is uniform and there is no

significant twist or warpage of the part, as expected since its laminate design is symmetric, balanced and quasi-isotropic. From the simulation it was also found that the trimming process releases residual stresses and the part springs back to its nominal shape to some extent.

### 5.1. Effect of the tool material

From the experiments it was found that the material of the tool has a significant effect on the spring-in angle of the parts. The parts manufactured from the INVAR tool experience on average less deformation compared to the parts manufactured from the steel or aluminium tools. This phenomenon was also observed by [16]. The specimens manufactured from the aluminium tool have a higher average spring-in angle compared to the parts manufactured from the steel tool (Table A.3). However, the standard deviation of the spring-in angle of the parts

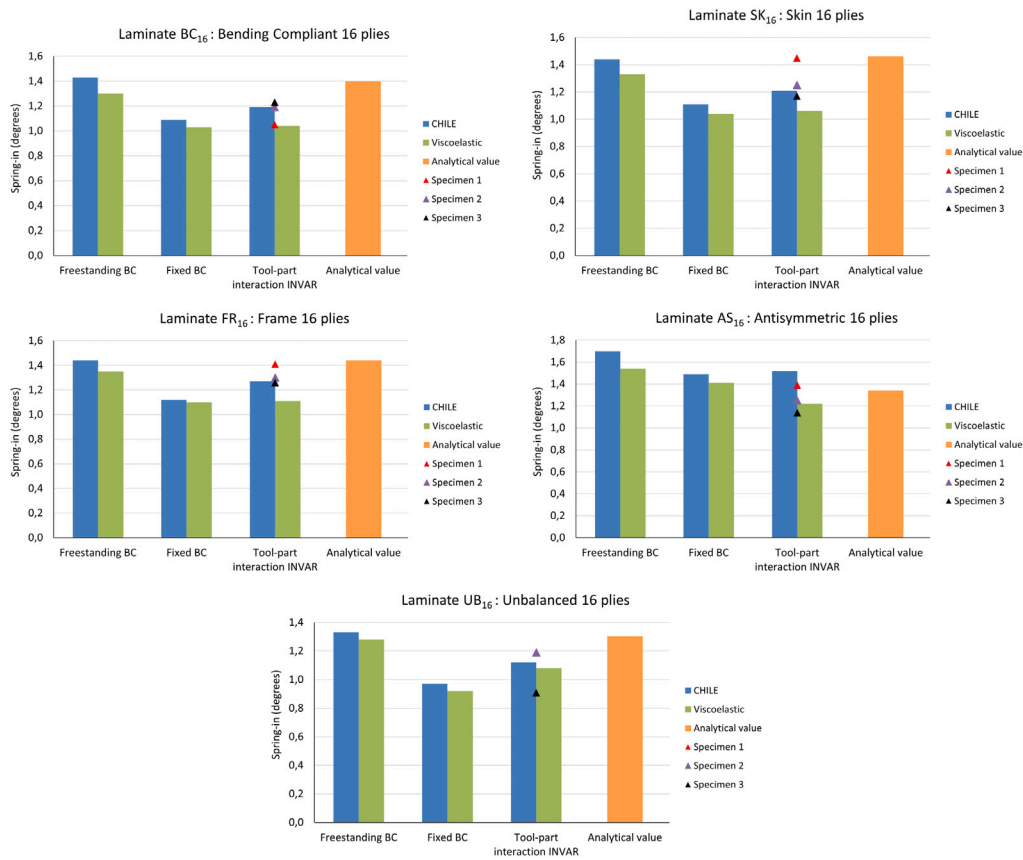


Fig. 16. Experimentally measured (specimen 1–3) and predicted spring-in angle of the 16 plies specimens manufactured with the INVAR tool and MRCC.

made from the steel and aluminium tool overlap. Consequently, a solid conclusion about which tool produces less distortion cannot be made even though that the CTE of the aluminium tool is significantly higher than that of the steel tool (Table 1). We postulate that the steel and aluminium tools produce similar spring-in angles for the BS<sub>16</sub>, ST<sub>16</sub> and the SP<sub>16</sub> laminate designs due to tool geometric and material non-linearities induced to the tools from the welding of the supporting substructure with the bended plate. These non-linearities exist also in the INVAR tool, however they do not affect significantly the spring-in angle of the part due to the very low CTE of the INVAR tool (Table 1). Due to this fact the INVAR alloy is the preferred choice by the industry to manufacture tools that produce parts of high dimensional accuracy.

### 5.2. Effect of the laminate design

The effect of the laminate design and thickness on the spring-in angle of the parts is investigated in relation to their bending stiffness  $D_{11}$  as these factors are coupled. Fig. 19 depicts the spring-in angle of the laminates, manufactured with the INVAR tool and MRCC, in relation to the bending stiffness  $D_{11}$ . As depicted in Fig. 19 the 24 plies laminates which have the highest  $D_{11}$  value experience the least average spring-in (below 1°) compared to the 8 and 16 plies laminates. The average spring-in of the 16 plies laminates (the group of laminates depicted in the middle of Fig. 19) is in the range of 1° to 1.3° which is below the 8 plies group if BC<sub>8</sub> is ignored, as due to its very low bending stiffness there is a large scatter of measurement data. Because the standard deviation of the laminates overlap in many cases (Tables A.1,A.2,A.4) only the qualitative conclusion can be made that the spring-in angle on the parts reduces as the bending stiffness  $D_{11}$  of the laminate increases which is also observed by other researchers [8,63]. Moreover, it is observed that as the bending stiffness  $D_{11}$  increases, the standard deviation of the measured spring-in angles reduces, indicating

that the laminate is less sensitive to manufacturing process or material variabilities.

Furthermore, as expected the anti-symmetric (AS) and heavily unbalanced (UB) laminates experience in addition to spring-in significant warpage or twist. Therefore, it is recommended to design symmetric and balanced laminates to avoid the coupling of the bending and twisting distortions of the laminate. Moreover, Eq. (1) cannot take into account the effect of thickness on the predicted spring-in angle of the part. It predicts the same spring-in angle for the bending stiff and compliant laminates (BS and BC) irrespective of the number of plies as depicted in Table A.1,A.2,A.4.

### 5.3. Effect of the curing cycle

The curing cycle proved to have a small effect on the spring-in angle of the parts for the two laminate designs (BS<sub>8</sub>, BC<sub>8</sub>) also manufactured with the “Fast” curing cycle. The BS<sub>8</sub> laminate design manufactured with the “Fast” curing cycle has a lower average spring-in value compared to the group manufactured with the MRCC (Table A.1). However, when excluding specimen 1 of the BS<sub>8</sub> group manufactured with the MRCC, which has significantly higher spring-in value compared to specimen 2 and 3, as depicted in Fig. 15 (the reason for this large deviation is not clear to the researchers), the average spring-in value of the MRCC group is lower compared to the “Fast” curing cycle (1.23° vs. 1.27°) and the standard deviations of the two groups do not overlap. Furthermore, both material models for the majority of the BCs investigated and Eq. (1) predict slightly higher spring-in angle for the “Fast” curing cycle compared to the MRCC (Table A.1). Therefore, it can be concluded that the “Fast” curing cycle which has an elevated curing temperature compared to the MRCC (195 °C vs. 180 °C) induces higher spring-in angle to the parts. This is expected when considering Eq. (1) and its dependence on  $\Delta T$ , as a greater difference of the curing

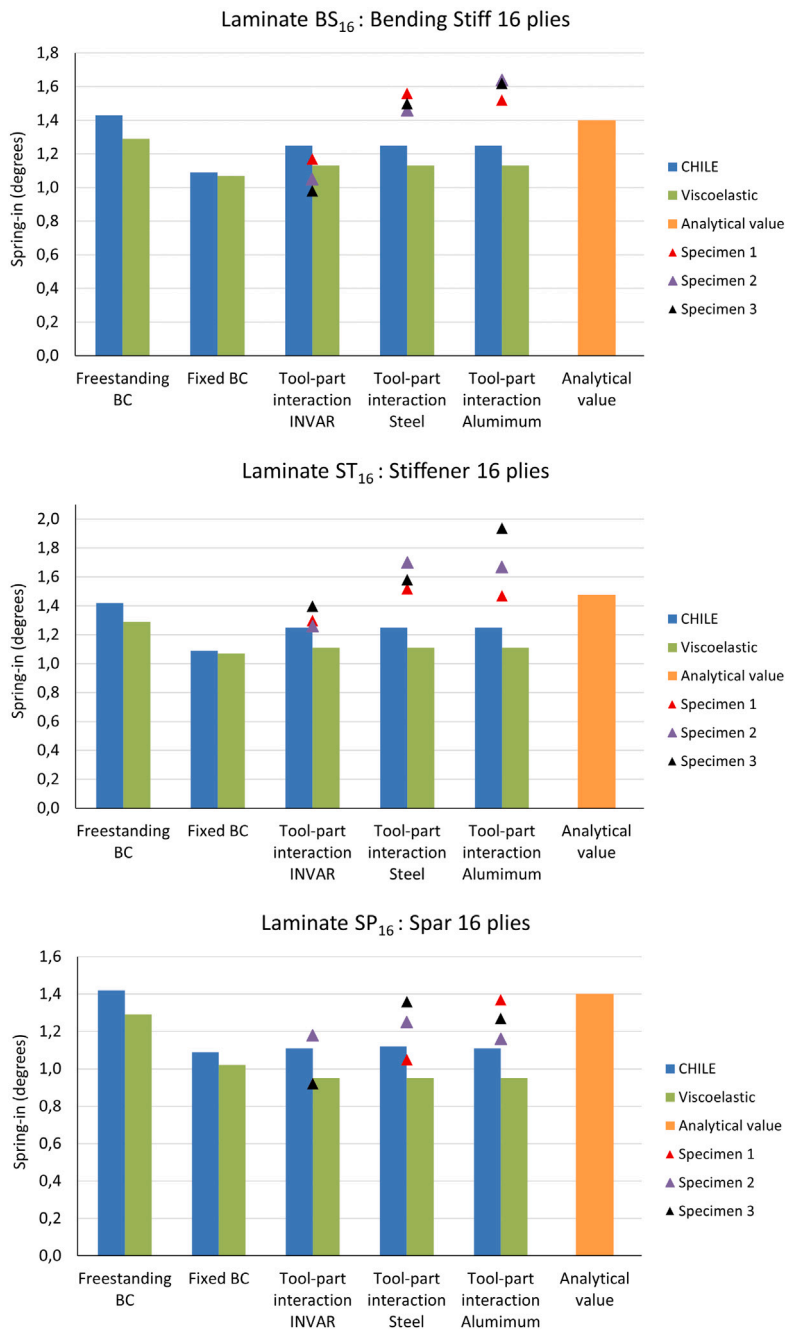


Fig. 17. Experimentally measured (specimen 1–3) and predicted spring-in angle of the 16 plies specimens manufactured with the INVAR, steel and aluminium tools.

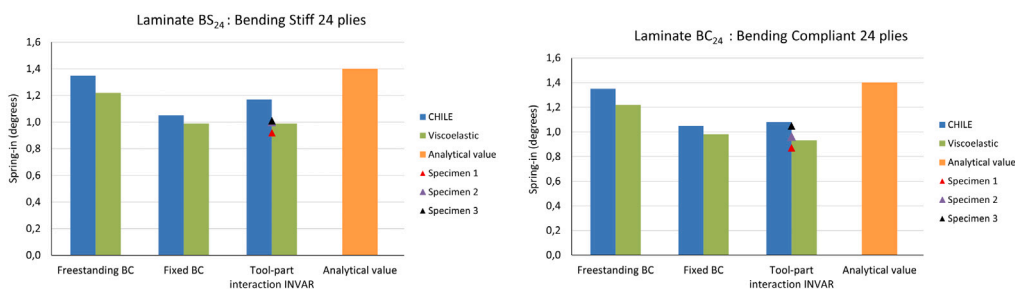


Fig. 18. Experimentally measured (specimen 1–3) and predicted spring-in angle of the 24 plies specimens manufactured.

temperature to room temperature will increase the induced spring-in angle (as  $CTE_T$  is small). However, further experimental validation is

needed for this case as the  $BC_8$  group suffers from a large scatter of the measurement data (which is believed to be due to its low bending

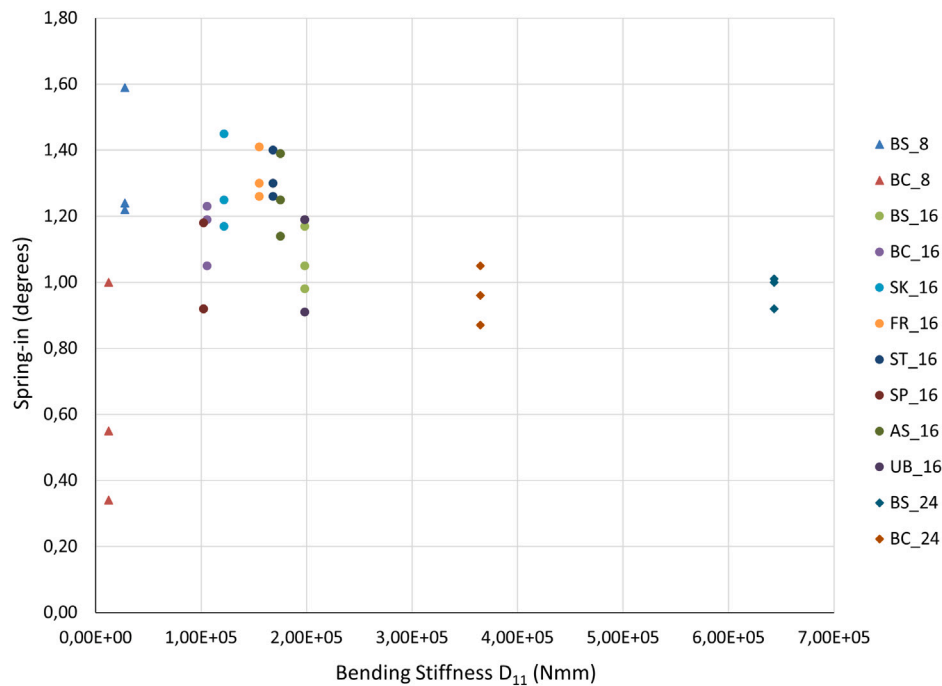


Fig. 19. Spring-in angle of the parts, manufactured with the INVAR tool and MRCC, in relation to their bending stiffness  $D_{11}$ .

stiffness that makes it prone to the bending and shear forces of the machining and handing operations) and a solid conclusion cannot be made even though the  $BC_8$  group manufactured with the “Fast” curing cycle has also slightly higher average spring-in value compared to the group manufactured from MRCC.

Moreover, by employing a heat transfer analysis prior to the spring-in analysis it was found for the 24 plies laminates that the non-uniform temperature field mapped to the spring-in analysis (Fig. 8) increases the agreement of the predicted spring-in angle in the range of  $0.04^\circ$  to  $0.08^\circ$  compared to the assumption of a homogeneous temperature field across the part. The greatest difference of temperature across the part predicted by the heat transfer analysis for the MRCC is below  $1^\circ\text{C}$ , which is expected due to low heating and cool down rates of the MRCC. However, the impact of employing a heat transfer analysis prior to the spring-in analysis would be greater for thicker parts (spar, wing root etc.) where the exothermic heat reaction generated by the resin is significant and for parts manufactured by curing cycles with high heating and cool down rates ( $> 3^\circ\text{C}$ ).

#### 5.4. Effect of the boundary conditions

Regarding the ability of the various boundary conditions to predict the deformed shape of the part, it was found for the modified CHILE model, that the agreement of the tool-part interaction simulation to the average spring-in angle is the best for half of the cases presented in Tables A.1,A.2,A.4 while for the rest cases the fixed BC has the best agreement to the experimental data. The freestanding BC proved to overestimate the spring-in angle of all the parts with the use of the CHILE material model. Concerning the viscoelastic material model each of the fixed BC and tool-part interaction simulation predict more accurately the average spring-in angle of 5 out of 14 cases investigated, while for the rest four cases the freestanding BC is the most accurate one.

Furthermore, for most of the cases the values for the tool-part interaction prediction lie between the fixed and freestanding BC cases. The fixed BC can be regarded as the case where the part is totally constrained by the tool which does not change its dimensions during the cycle. Therefore, the minimum spring-in should be expected from this

case. On the contrary at the freestanding BC the part can expand and contract freely and this case accounts for the upper limit of the expected distortions. This was also observed by Svanberg, who concluded that the most accurate BC to be employed is the tool-part simulation [23]. Moreover, it was found that the dependence of the CoF on degree of cure does not affect the simulation results. A number of cases were also run having a fixed CoF  $\mu = 0.3$  and the results were almost identical to the tool-part simulations employing Eq. (14). Thus, it can be assumed that the CoF is constant during the analysis without reducing simulation accuracy [5,14].

However, as depicted in Fig. 17 and Table A.3 the tool part-simulation employed here cannot capture the effect of the tool material on spring-in sufficiently for the case of the steel and aluminium tool. It is believed, this is due to the geometric and material non-linearities of the tools which could not be included in the modelling.

#### 5.5. Effect of the material models

Comparing the two material models for a given laminate design regarding their ability to predict the deformed shape of the part, the viscoelastic model is the most accurate as with the right combination of BC its prediction is closer to the average spring-in angle measured for most of the cases studied (12 out of 14). Regardless of the laminate design the viscoelastic model is the most accurate material model when the freestanding BC (in all cases studied) and the tool-part interaction (9 out of 14) is employed. When the fixed BC is used, the modified CHILE material model performs equally well with the viscoelastic in the sense that it can predict more accurately half of the cases investigated. Overall it can be stated, that the modified CHILE material model overestimates the spring-in angle in the majority of the cases studied, which is in agreement with the work presented in the literature [41,64].

As depicted in Figs. 15,16,17 and Fig. 18 the viscoelastic material model predicts a lower spring-in angle compared to the modified CHILE material model for the same boundary conditions. This can be attributed to the difference in the instantaneous modulus of the two material models as presented in Fig. 13 and to the inability of the CHILE material model to account for the time dependent factors, such as stress relaxation, that affect the distortion of the parts from gelation of the structure to cool down.

However, the computational time required by the viscoelastic material model is approximately 2.5 times greater than the CHILE material model mainly because of the large number of small time increments required to complete the simulations. In addition, the computational time is increased by the increased number of state variables that have to be read from the memory, updated by the material constitutive equation and stored back in memory at every time increment [53].

Furthermore, it was found that the result of Eq. (1) overestimate the average spring-in angle for most of the cases investigated and its result is close to the prediction of the modified CHILE material model with the use of the freestanding BC. This is expected as Eq. (1) cannot take into account the effect of extrinsic parameters on PID [34] as also observed by Svanberg [23].

### 5.6. Potential sources of error

The deviation of the simulation results from the experimental measurements can be attributed to a number of factors relevant to the modelling assumptions and to the experimental process performed.

#### 5.6.1. Modelling assumptions

Starting from the modelling assumptions, the simulation framework developed was applied from the gelation of the structure. Therefore, fabric compaction, permeability and resin flow were not considered in the modelling approach. This leads to the assumption of homogeneous fibre volume fraction and void content in the part during the cure. However, the distribution of the resin in the part at the end of the infusion process is inhomogeneous to some extent depending among other factors on the local part radius, stacking sequence, positioning of the resin flow medium across the part, fibre bridging, wrinkling and reorientation etc. [65]. These factors cause resin rich and resin starved areas resulting in property gradients in the consolidated laminate affecting process induced distortions and residual stresses. While the assumption of stress-free laminate having homogeneous fibre volume fraction before the gelation of the structure ( $\alpha = 0.66$ ) reduces the complexity of the simulation making it also faster to run, it also reduces its accuracy as a small amount of residual stresses might also be developed before that point, slightly affecting the distortion of the structure.

In the absence of specific material data at the application of the simulation framework material constants published in the literature were used. The Poisson's coefficients, the shear modulus and transverse modulus of AS4 fibre were used as shown in Table 2. This might impair the accuracy of the simulation and be responsible for some of the discrepancy between the calculations and the experiment, the exact magnitude of which is not known.

Also, to calculate the conductivity of the EPIKOTE™ System 600 at every time increment the material constants of the EPON 862/EPIKURE 3300 epoxy system were used. The two resin systems should have approximately the same conductivity in the liquid state. However, the conductivity of the two systems increasingly deviates as the degree of cure increases due to the difference in the crosslinking of the two systems, which is represented by the different recommended cure cycles of the two systems (2 hours at 180°C for the EPIKOTE™ System 600, 90 min at 82°C + 90 min at 150°C for the EPON 862/EPIKURE 3300 epoxy system). In addition, the material constants of the conductivity and specific heat capacity of AS4 fibre were used.

Nevertheless, the effect of using these material constants in the heat transfer simulation is considered to be small. As was observed in the experiment and in the simulation the difference in the spring-in angle of the specimens manufactured with the MRCC and "Fast" curing cycle is small, despite the fact that these curing cycles were substantially different. Consequently, we postulate that a difference in the conductivity would result in a temperature field difference in the part which would not substantially affect the spring-in angle of the specimens.

Moreover, for the 8 and 16 plies specimens, a homogeneous temperature field was considered across the parts due to the small wall thickness of the specimens and the low heating and cool down rates. However, small temperature gradients exist in the structure due to the positioning of the tool in the oven and the exothermic heat reaction of the resin, resulting in property gradients which affect the distortion of the structure. For the 24 ply specimens even though a heat transfer analysis was performed prior to the spring-in analysis the heat transfer coefficient was approximated and not measured or calculated.

Furthermore, the viscoelastic model was based on the assumption of thermo-rheological simplicity, which is considered by Simon et al. [66] a good approximation for modelling the evolution of viscoelastic properties after the gelation of the structure. This implies that the retardation spectrum is assumed to not vary with temperature or degree of cure but is simply shifted along the time axis. Plazek et al. suggest this is valid for the time-temperature superposition, but it is not strictly valid for the time-cure superposition [67]. However, consideration of thermo-rheologically complex material behaviour would require further material characterisation.

In addition, all simulations were run from the nominal geometry (having an angle of 90°) so the distortion of the tools is not included. This may induce some error to simulation results as different geometries produce different amounts of spring-in, known as non-linearity in the tool compensation process [68]. Finally, the biaxial NCF was modelled as two UD plies, neglecting the effect of stitching of the fabric and bundle-bundle nesting effects.

#### 5.6.2. Experimental uncertainties

Regarding the experimental factors or uncertainties that affect the parts produced, it was found that the steel and aluminium tools did not have the same included angle along their length. More specifically, by splitting the tool surface in half and fitting two planes to the surface instead of one a difference in the included angle of 0.14° was found for the steels and aluminium tools. In other words, if a part was manufactured on the right side of the aluminium tool would have a difference of 0.14° compared to the same part manufactured on the left side under the same conditions. Unfortunately, this was not known during the experiment and is not able to trace back the error to the respective specimens.

Moreover, even though the plies were cut in the press from the carbon fabric roll with the use of a custom made die, which ensured the accurate dimensions of the patches, the stacking sequence of the parts was manufactured manually on the tools without any laser projection method. This may lead to fibre reorientation during the handling and bagging operations affecting the induced distortions.

From the experiment, corner thickening of the specimens was also observed. The average value of the corner thickness for each laminate design is presented in Table A.5 and in some cases the corner is more than 1 mm thicker than average thickness of the flanges of the parts. This was not taken into account in the simulation. However, its effect on the induced distortion of the part is thought to be small [23]. In addition as depicted in Table 3 the average thickness of the flanges of the specimens is greater than their nominal value (approximately +0.14 mm, +0.13 mm and +0.17 mm for the 8, 16 and 24 ply specimens respectively). This might be due to material variability as well as not perfect fibre compaction and was not taken into account in the modelling.

Also, the temperature profile depicted in Fig. 7 could not be replicated in every manufacturing run. The infusion and dwell times as well as heating and cool down rates differ at each case, depending on the position of the tool in the oven, the number of the tools in the oven and setting of the oven (speed of ventilation fan etc.). Nevertheless, it was attempted to keep heating and cool down rates below 2.5° C/min and let the parts cure for a least 2 h at MRCC. The difference between the temperature profiles that the tools experience under the same curing cycle is more evident when the aluminium tool is placed in the

oven along with the steel and INVAR tool. Due to its reduced thermal mass compared to the other tools, the parts from the aluminium tool reach the curing temperature sooner and are thus kept at the curing temperature longer until the two hour cycle is completed for the other slowest parts in the oven. This may lead to a higher final degree of cure at the end of the cycle compared to the parts made from steel or INVAR tools.

Furthermore, the fixture of the parts to the CMM (Fig. 5) could potentially induce error to the measurement of their spring-in angle. This is the reason why the eight ply specimens was chosen not to be measured in the CMM. With the use of the 3D scanner this error can be avoided, as it is a contact-less measurement method, however the accuracy of the 3D scanner used in the experiment was 0.2 mm.

In addition to the above presented factors, the data reduction method used to calculate the spring-in angle of the parts both for the experiment and simulation (Gaussian best fit of planes to the CMM, 3D scanner or distorted mesh data) is a potential source of error. This method is less efficient as the twist or warpage of the part increases as in the case of the  $AS_{16}$  laminate because the average deviation of plane to the data increases. In those cases it is recommended that more than one plane should be fitted to the surface to reduce the deviation. Consequently, those parts should be described by more than one spring-in angle along their length or an alternative twist factor. Especially for parts that do not contain angled sections a completely different approach might be necessary to characterize the induced distortion (contour plot of mesh deviation from CAD etc.).

## 6. Conclusions

From the research presented it can be concluded that the material of the tool has a significant effect on the spring-in angle of the parts. The parts manufactured with the INVAR tool experience on average less deformation compared to the parts manufactured with the steel or aluminium tools. Consequently, tool-part interaction plays an important role even in the manufacturing of these simple L-shape structures. Its effect is more evident when there is a large difference between the coefficient of thermal expansion of the laminate and the tool.

Furthermore, it was found that the spring-in angle on the parts reduces as the bending stiffness,  $D_{11}$ , of the laminate increases, as the 24 plies specimens experience the least average spring-in angle compared to the other laminate groups. Moreover, symmetric and balanced laminates are recommended to avoid the coupling of the bending and twisting distortions of the laminate.

It was found that the “Fast” curing cycle which has an elevated curing temperature compared to the MRCC (195 °C vs. 180 °C) induces higher spring-in angle of the parts, which was also predicted by the simulation and Eq. (1). However, the increase of the spring-in angle of the parts due to the “Fast” curing cycle is considered small, compared to the manufacturing time saved by the use of this curing cycle.

The heat transfer analysis performed for the 24 plies laminates prior to the spring-in analysis was found to increase the accuracy of the predicted spring-in angle in the range of 0.04° to 0.08° compared to the assumption of a homogeneous temperature field across the part.

A model that includes a tool-part interaction was found to be more accurate in predicting PID of composites than the models employing the fixed and freestanding BCs. The spring-in angles predicted by the tool-part interaction model were usually between the bounds defined by the use of the fixed (lower bound) and freestanding (upper bound) boundary condition. The use of the cure-dependent coefficient of friction was found to have negligible effect on the results while adding significant computational costs.

Finally, it was found that the modified CHILE material model overestimates the spring-in angle for the majority of the cases studied. Eq. (1) also overestimates the average spring-in angle of most of the cases and its result is close to the prediction of the CHILE material

**Table A.1**

Measured and predicted spring-in angle (°) of the 8 plies specimens manufactured with the MRCC and Fast curing cycle. The parts were manufactured from the INVAR tool and measured with the 3D scanner.

Laminate	Curing cycle	$BS_8$		$BC_8$	
		MRCC	Fast	MRCC	Fast
CHILE	Free	1.43	1.48	1.42	1.47
	Fixed	1.09	1.11	1.08	1.10
	Tool	1.33	1.33	1.24	1.29
Viscoel.	Free	1.28	1.31	1.29	1.32
	Fixed	1.07	1.05	1.06	1.05
	Tool	1.26	1.30	1.10	1.18
Exp.	Spec.1	1.59	1.24	0.34	0.48
	Spec.2	1.22	1.28	1.00	0.62
	Spec.3	1.24	1.28	0.55	0.81
	Average	1.35	1.27	0.63	0.64
	St.Dev.	0.21	0.02	0.34	0.17
Radford Eq. (1)		1.40	1.44	1.40	1.44

model with the use of the freestanding boundary conditions. The viscoelastic material model is proposed to be employed for an accurate prediction of process induced distortions of composites, as it can take into account the time dependent factors, such as stress relaxation, that affect the distortion of the parts from gelation of the structure through to cool down.

## CRedit authorship contribution statement

**Neoklis Traiforos:** Writing – original draft, Investigation, Data curation, Software, Formal analysis, Methodology, Visualization. **Mikhail Matveev:** Supervision, Writing – review & editing, Methodology, Conceptualization. **Dimitrios Chronopoulos:** Supervision, Funding acquisition, Conceptualization, Methodology. **Thomas Turner:** Supervision, Project administration, Writing – review & editing, Methodology, Conceptualization.

## Declaration of competing interest

The authors declare that they have no known competing financial interests or personal relationships that could have appeared to influence the work reported in this paper.

## Data availability

Data will be made available on request.

## Acknowledgements

This work has received funding from the European Union’s Horizon 2020 research and innovation programme under the Marie Skłodowska-Curie grant agreement No 764650. It is part of the OptiMACS project performing research in the field of optimisation of multifunctional aerospace composite structures. The authors would like to thank Dr. Tareq Hasson from Hexion Germany GmbH for providing the resin system necessary to conduct the experiment. Furthermore, the authors would like to acknowledge the contribution of Mr. Roland Bernicke and his team from Teijin Carbon Europe GmbH as well as the contribution of Ralf Trost from Premium AEROTEC GmbH that coordinated the shipment of the carbon fabric. Finally, the authors would like to thank especially, Mr. Patrik Runeberg from Premium AEROTEC GmbH for his continuous support to this research.

## Appendix. Tabulated results

See Tables A.1–A.5.



**Table A.2**

Measured and predicted spring-in angle (°) of the 16 plies specimens manufactured with the MRCC and INVAR tool. The parts were measured with the CMM.

Laminate		$BS_{16}$	$BC_{16}$	$SK_{16}$	$FR_{16}$	$ST_{16}$	$SP_{16}$	$AS_{16}$	$UB_{16}$
CHILE	Free	1.43	1.43	1.44	1.44	1.42	1.42	1.70	1.33
	Fixed	1.09	1.09	1.11	1.12	1.09	1.09	1.49	0.97
	Tool	1.25	1.19	1.21	1.27	1.25	1.11	1.52	1.12
Viscoel.	Free	1.29	1.30	1.33	1.35	1.29	1.29	1.54	1.28
	Fixed	1.07	1.03	1.04	1.10	1.07	1.02	1.41	0.92
	Tool	1.13	1.04	1.06	1.11	1.11	0.95	1.22	1.08
Exp.	Spec.1	1.17	1.05	1.45	1.41	1.30	0.92	1.39	1.19
	Spec.2	1.05	1.19	1.25	1.30	1.26	1.18	1.25	1.19
	Spec.3	0.98	1.23	1.17	1.26	1.40	0.92	1.14	0.91
	Average	1.07	1.16	1.29	1.32	1.32	1.01	1.26	1.10
	St.Dev.	0.10	0.09	0.14	0.08	0.07	0.15	0.13	0.16
Radford Eq. (1)		1.40	1.40	1.46	1.44	1.48	1.40	1.34	1.30

**Table A.3**

Measured and predicted spring-in angle (°) of the 16 plies laminate groups manufactured also with the steel and aluminium tools. The parts were measured with the CMM and manufactured with the MRCC.

Laminate	$BS_{16}$		$ST_{16}$		$SP_{16}$		
	Steel	Aluminium	Steel	Aluminium	Steel	Aluminium	
CHILE	1.25	1.25	1.25	1.25	1.12	1.11	
Viscoel.	1.13	1.13	1.11	1.11	0.95	0.95	
Exp.	Spec.1	1.56	1.52	1.52	1.47	1.05	1.37
	Spec.2	1.46	1.64	1.70	1.67	1.25	1.16
	Spec.3	1.50	1.62	1.58	1.94	1.36	1.27
	Average	1.51	1.59	1.60	1.69	1.22	1.27
	St.Dev.	0.05	0.06	0.09	0.24	0.16	0.11

**Table A.4**

Measured and predicted spring-in angle (°) of the 24 plies specimens manufactured with the MRCC and INVAR tool. The parts were measured with the CMM.

Laminate		$BS_{24}$	$BC_{24}$
CHILE	Free	1.35	1.35
	Fixed	1.05	1.05
	Tool	1.17	1.08
Viscoel.	Free	1.22	1.22
	Fixed	0.99	0.98
	Tool	0.99	0.93
Exp.	Spec.1	0.92	0.87
	Spec.2	1.00	0.96
	Spec.3	1.01	1.05
	Average	0.98	0.96
	St.Dev.	0.05	0.09
Radford Eq. (1)		1.40	1.40

**Table A.5**

Thickness of the specimens manufactured.

Laminate	t (mm)	$t_{corner}$ (mm)
$BS_8$	1.62±0.06	2.32±0.21
$BC_8$	1.60±0.05	1.97±0.12
$BS_{16}$	3.08±0.08	4.54±0.59
$BC_{16}$	3.07±0.09	3.77±0.19
$SK_{16}$	3.04±0.07	4.15±0.13
$FR_{16}$	3.09±0.08	4.20±0.18
$ST_{16}$	3.04±0.08	4.59±0.53
$SP_{16}$	3.06±0.08	3.79±0.39
$AS_{16}$	3.12±0.11	4.32±0.23
$UB_{16}$	3.05±0.08	4.64±0.32
$BS_{24}$	4.62±0.09	6.13±0.25
$BC_{24}$	4.56±0.10	5.67±0.08

**References**

[1] Albert C, Fernlund G. Spring-in and warpage of angled composite laminates. *Compos Sci Technol* 2002;62(14):1895–912. [http://dx.doi.org/10.1016/S0266-3538\(02\)00105-7](http://dx.doi.org/10.1016/S0266-3538(02)00105-7).

[2] Ding A, Wang J, Li S. Understanding process-induced spring-in of L-shaped composite parts using analytical solution. *Compos Struct* 2020;250:112629. <http://dx.doi.org/10.1016/j.compstruct.2020.112629>.

[3] Twigg G, Poursartip A, Fernlund G. Tool-part interaction in composites processing. Part I: experimental investigation and analytical model. *Composites A* 2004;35(1):121–33. [http://dx.doi.org/10.1016/S1359-835X\(03\)00131-3](http://dx.doi.org/10.1016/S1359-835X(03)00131-3).

[4] Kappel E, Stefaniak D, Hühne C. Process distortions in prepreg manufacturing – an experimental study on CFRP L-profiles. *Compos Struct* 2013;106:615–25. <http://dx.doi.org/10.1016/j.compstruct.2013.07.020>.

[5] Khoun L, de Oliveira R, Michaud V, Hubert P. Investigation of process-induced strains development by fibre bragg grating sensors in resin transfer moulded composites. *Composites A* 2011;42:274–82. <http://dx.doi.org/10.1016/j.compositesa.2010.11.013>.

[6] Fernlund G, Rahman N, Courdji R, Bresslauer M, Poursartip A, Willden K, et al. Experimental and numerical study of the effect of cure cycle, tool surface, geometry, and lay-up on the dimensional fidelity of autoclave-processed composite parts. *Composites A* 2002;33(3):341–51. [http://dx.doi.org/10.1016/S1359-835X\(01\)00123-3](http://dx.doi.org/10.1016/S1359-835X(01)00123-3).

[7] Wisnom M, Gigliotti M, Ersoy N, Campbell M, Potter K. Mechanisms generating residual stresses and distortion during manufacture of polymer-matrix composite structures. *Composites A* 2006;37(4):522–9. <http://dx.doi.org/10.1016/j.compositesa.2005.05.019>, Internal Stresses in Polymer Composites.

[8] Hörberg E, Nyman T, Åkermo M, Hallström S. Thickness effect on spring-in of prepreg composite L-profiles – an experimental study. *Compos Struct* 2019;209:499–507. <http://dx.doi.org/10.1016/j.compstruct.2018.10.090>.

[9] Ding A, Fang S, Li X, Sun L, Wang J, Chen H. Experimental and numerical investigation of tool-part interaction on the process-induced distortions in composite structures. *Compos Struct* 2022;279:114871. <http://dx.doi.org/10.1016/j.compstruct.2021.114871>.

[10] Bellini C, Sorrentino L. Analysis of cure induced deformation of CFRP U-shaped laminates. *Compos Struct* 2018;197:1–9. <http://dx.doi.org/10.1016/j.compstruct.2018.05.038>.

[11] Bellini C, Sorrentino L, Polini W, Corrado A. Spring-in analysis of CFRP thin laminates: numerical and experimental results. *Compos Struct* 2017;173:17–24. <http://dx.doi.org/10.1016/j.compstruct.2017.03.105>.

[12] Çiçek KF, Erdal M, Kayran A. Experimental and numerical study of process-induced total spring-in of corner-shaped composite parts. *J Compos Mater* 2017;51(16):2347–61. <http://dx.doi.org/10.1177/0021998316669993>.

[13] Mezeix L, Seman A, Nasir M, Aminanda Y, Rivai A, Castanié B, et al. Spring-back simulation of unidirectional carbon/epoxy flat laminate composite manufactured through autoclave process. *Compos Struct* 2015;124:196–205. <http://dx.doi.org/10.1016/j.compstruct.2015.01.005>.

[14] Çınar K, Ersoy N. 3D finite element model for predicting manufacturing distortions of composite parts. *J Compos Mater* 2016;50(27):3791–807. <http://dx.doi.org/10.1177/0021998315625789>.

[15] Twigg G, Poursartip A, Fernlund G. Tool-part interaction in composites processing. Part II: numerical modelling. *Composites A* 2004;35(1):135–41. [http://dx.doi.org/10.1016/S1359-835X\(03\)00132-5](http://dx.doi.org/10.1016/S1359-835X(03)00132-5).

[16] Kappel E. Forced-interaction and spring-in – relevant initiators of process-induced distortions in composite manufacturing. *Compos Struct* 2016;140:217–29. <http://dx.doi.org/10.1016/j.compstruct.2016.01.016>.

[17] Zeng X, Raghavan J. Role of tool-part interaction in process-induced warpage of autoclave-manufactured composite structures. *Composites A* 2010;41:1174–83. <http://dx.doi.org/10.1016/j.compositesa.2010.04.017>.

[18] de Oliveira R, Lavanchy S, Chatton R, Costantini D, Michaud V, Salathé R, et al. Experimental investigation of the effect of the mould thermal expansion on the development of internal stresses during carbon fibre composite processing. *Composites A* 2008;39(7):1083–90. <http://dx.doi.org/10.1016/j.compositesa.2008.04.011>.

[19] Al-Dhaheri M, Khan K, Umer R, van Liempt F, Cantwell W. Process-induced deformation in U-shaped honeycomb aerospace composite structures. *Compos Struct* 2020;248:112503. <http://dx.doi.org/10.1016/j.compstruct.2020.112503>.

[20] Kappel E. Spring-in of curved CFRP/foam-core sandwich structures. *Compos Struct* 2015;128:155–64. <http://dx.doi.org/10.1016/j.compstruct.2015.03.058>.

[21] Al-Dhaheri M, Khan K, Umer R, van Liempt F, Cantwell W. Process induced deformations in composite sandwich panels using an in-homogeneous layup design. *Composites A* 2020;137:106020. <http://dx.doi.org/10.1016/j.compositesa.2020.106020>.

[22] Mahadik Y, Potter K. Experimental investigation into the thermoelastic spring-in of curved sandwich panels. *Composites A* 2013;49:68–80. <http://dx.doi.org/10.1016/j.compositesa.2013.02.006>.

[23] Svanberg JM. Predictions of manufacturing induced shape distortions. *Lulea University of Technology*; 2002.

[24] Wisnom MR, Potter KD, Ersoy N. Shear-lag analysis of the effect of thickness on spring-in of curved composites. *J Compos Mater* 2007;41(11):1311–24. <http://dx.doi.org/10.1177/0021998306068072>.

[25] Ding A, Li S, Wang J, Ni A. A new analytical solution for spring-in of curved composite parts. *Compos Sci Technol* 2017;142:30–40. <http://dx.doi.org/10.1016/j.compscitech.2017.01.024>.

- [26] Dong C. Modeling the process-induced dimensional variations of general curved composite components and assemblies. *Composites A* 2009;40(8):1210–6. <http://dx.doi.org/10.1016/j.compositesa.2009.05.013>, Special Issue: 15th French National Conference on Composites - JNC15.
- [27] Kappel E, Stefaniak D, Fernlund G. Predicting process-induced distortions in composite manufacturing – a pheno-numerical simulation strategy. *Compos Struct* 2015;120:98–106. <http://dx.doi.org/10.1016/j.compstruct.2014.09.069>.
- [28] Chen W, Zhang D. A micromechanics-based processing model for predicting residual stress in fiber-reinforced polymer matrix composites. *Compos Struct* 2018;204:153–66. <http://dx.doi.org/10.1016/j.compstruct.2018.07.016>.
- [29] Ding A, Li S, Wang J, Ni A, Zu L. A new path-dependent constitutive model predicting cure-induced distortions in composite structures. *Composites A* 2017;95:183–96. <http://dx.doi.org/10.1016/j.compositesa.2016.11.032>.
- [30] Abouhamzeh M, Sinke J, Jansen K, Benedictus R. A new procedure for thermo-viscoelastic modelling of composites with general orthotropy and geometry. *Compos Struct* 2015;133:871–7. <http://dx.doi.org/10.1016/j.compstruct.2015.08.050>.
- [31] Arafath ARA, Vaziri R, Poursartip A. Closed-form solution for process-induced stresses and deformation of a composite part cured on a solid tool: Part I – flat geometries. *Composites A* 2008;39:1106–17. <http://dx.doi.org/10.1016/j.compositesa.2008.04.009>.
- [32] Arafath ARA, Vaziri R, Poursartip A. Closed-form solution for process-induced stresses and deformation of a composite part cured on a solid tool: Part II – curved geometries. *Composites A* 2009;40:1545–57. <http://dx.doi.org/10.1016/j.compositesa.2009.01.009>.
- [33] Chen J, Wang J, Li S, Wang C, Ding A. Analytical solutions for process-induced spring-in of U-shaped composite parts. *Thin-Walled Struct* 2021;169:108425. <http://dx.doi.org/10.1016/j.tws.2021.108425>.
- [34] Radford DW, Rennick TS. Separating sources of manufacturing distortion in laminated composites. *J Reinf Plast Compos* 2000;19(8):621–41. <http://dx.doi.org/10.1177/073168440001900802>.
- [35] Kappel E, Stefaniak D, Spröwitz T, Hühne C. A semi-analytical simulation strategy and its application to warpage of autoclave-processed CFRP parts. *Composites A* 2011;42:1985–94. <http://dx.doi.org/10.1016/j.compositesa.2011.09.001>.
- [36] Johnston AA. An integrated model of the development of process-induced deformation in autoclave processing of composite structures (Ph.D. thesis). In: *Retrospective Theses and Dissertations, 1919-2007*, University of British Columbia; 1997. <http://dx.doi.org/10.14288/1.0088805>.
- [37] Wang Q, Li T, Yang X, Wang K, Wang B, Ren M. Prediction and compensation of process-induced distortions for L-shaped 3D woven composites. *Composites A* 2021;141:106211. <http://dx.doi.org/10.1016/j.compositesa.2020.106211>.
- [38] Zappino E, Zobeiry N, Petrolo M, Vaziri R, Carrera E, Poursartip A. Analysis of process-induced deformations and residual stresses in curved composite parts considering transverse shear stress and thickness stretching. *Compos Struct* 2020;241:112057. <http://dx.doi.org/10.1016/j.compstruct.2020.112057>.
- [39] Kravchenko OG, Kravchenko SG, Pipes RB. Cure history dependence of residual deformation in a thermosetting laminate. *Composites A* 2017;99:186–97. <http://dx.doi.org/10.1016/j.compositesa.2017.04.006>.
- [40] Moretti L, Castanié B, Bernhart G, Olivier P. Characterization and modelling of cure-dependent properties and strains during composites manufacturing. *J Compos Mater* 2020;54(22):3109–24. <http://dx.doi.org/10.1177/0021998320912470>.
- [41] Chen W, Zhang D. Improved prediction of residual stress induced warpage in thermoset composites using a multiscale thermo-viscoelastic processing model. *Composites A* 2019;126:105575. <http://dx.doi.org/10.1016/j.compositesa.2019.105575>.
- [42] Ersoy N, Garstka T, Potter K, Wisnom MR, Porter D, Stringer G. Modelling of the spring-in phenomenon in curved parts made of a thermosetting composite. *Composites A* 2010;41:410–8. <http://dx.doi.org/10.1016/j.compositesa.2009.11.008>.
- [43] Liu C, Shi Y. A thermo-viscoelastic analytical model for residual stresses and spring-in angles of multilayered thin-walled curved composite parts. *Thin-Walled Struct* 2020;152:106758. <http://dx.doi.org/10.1016/j.tws.2020.106758>.
- [44] Liu X, Guan Z, Wang X, Jiang T, Geng K, Li Z. Study on cure-induced residual stresses and spring-in deformation of L-shaped composite laminates using a simplified constitutive model considering stress relaxation. *Compos Struct* 2021;272:114203. <http://dx.doi.org/10.1016/j.compstruct.2021.114203>.
- [45] Zhang J, Zhang M, Li S, Pavier M, Smith D. Residual stresses created during curing of a polymer matrix composite using a viscoelastic model. *Compos Sci Technol* 2016;130:20–7. <http://dx.doi.org/10.1016/j.compscitech.2016.05.002>.
- [46] Ding A, Li S, Sun J, Wang J, Zu L. A thermo-viscoelastic model of process-induced residual stresses in composite structures with considering thermal dependence. *Compos Struct* 2016;136:34–43. <http://dx.doi.org/10.1016/j.compstruct.2015.09.014>.
- [47] Benavente M, Marcin L, Courtois A, Lévesque M, Ruiz E. Numerical analysis of viscoelastic process-induced residual distortions during manufacturing and post-curing. *Composites A* 2018;107:205–16. <http://dx.doi.org/10.1016/j.compositesa.2018.01.005>.
- [48] Poon H, Ahmad MF. A material point time integration procedure for anisotropic, thermo rheologically simple, viscoelastic solids. *Comput Mech* 1998;21(3):236–42. <http://dx.doi.org/10.1007/s004660050298>.
- [49] Fiorina M, Seman A, Castanie B, Ali K, Schwob C, Mezeix L. Spring-in prediction for carbon/epoxy aerospace composite structure. *Compos Struct* 2017;168:739–45. <http://dx.doi.org/10.1016/j.compstruct.2017.02.074>.
- [50] Kappel E, Stefaniak D, Holzrüter D, Hühne C, Sinapius M. Manufacturing distortions of a CFRP box-structure – a semi-numerical prediction approach. *Composites A* 2013;51:89–98. <http://dx.doi.org/10.1016/j.compositesa.2013.04.003>.
- [51] Kappel E. A zone-based approach to predict process-induced distortions of composite structures based on a 'spring-in reference curve'. *Compos Struct* 2019;209:143–9. <http://dx.doi.org/10.1016/j.compstruct.2018.10.045>.
- [52] Wucher B, Lani F, Pardoën T, Bailly C, Martiny P. Tooling geometry optimization for compensation of cure-induced distortions of a curved carbon/epoxy C-spar. *Composites A* 2014;56:27–35. <http://dx.doi.org/10.1016/j.compositesa.2013.09.010>.
- [53] Traiforos N, Turner T, Runeberg P, Fernass D, Chronopoulos D, Glock F, et al. A simulation framework for predicting process-induced distortions for precise manufacturing of aerospace thermoset composites. *Compos Struct* 2021;275:114465. <http://dx.doi.org/10.1016/j.compstruct.2021.114465>.
- [54] EPIKOTE system 600 and mixing services for high performance composite structures. In: *Product bulletin, HEXION*.
- [55] *Delivery Programme and Characteristics for Tenax® ims65 Filament Yarn*. Toho Tenax; 2010. <https://www.gom.com/en/products/gom-inspect-suite>.
- [56] <https://www.gom.com/en/products/gom-inspect-suite>.
- [57] Weiland J. EPS600 charakterisierung: Abschlussbericht. TUM Lehrstuhl für Carbon Composites; 2017.
- [58] COMPRO Model Documentation v1.3., Convergent Manufacturing Technologies.
- [59] Twigg G, Poursartip A, Fernlund G. An experimental method for quantifying tool-part shear interaction during composites processing. *Compos Sci Technol* 2003;63(13):1985–2002. [http://dx.doi.org/10.1016/S0266-3538\(03\)00172-6](http://dx.doi.org/10.1016/S0266-3538(03)00172-6).
- [60] Ersoy N, Potter K, Wisnom MR, Clegg MJ. An experimental method to study the frictional processes during composites manufacturing. *Composites A* 2005;36(11):1536–44. <http://dx.doi.org/10.1016/j.compositesa.2005.02.010>.
- [61] Kaushik V, Raghavan J. Experimental study of tool-part interaction during autoclave processing of thermoset polymer composite structures. *Composites A* 2010;41(9):1210–8. <http://dx.doi.org/10.1016/j.compositesa.2010.05.003>.
- [62] *Abaqus analysis user's guide version 6.14*. Dassault Systemes Simulia Corp; 2014.
- [63] Zhang G, Wang J, Ni A, Hu H, Ding A, Li S. Process-induced deformation of L-shaped variable-stiffness composite structures during cure. *Compos Struct* 2019;230(111461). <http://dx.doi.org/10.1016/j.compstruct.2019.111461>.
- [64] Nielsen MW, Schmidt JW, Hattel JH, Andersen TL, Markussen CM. In situ measurement using FBGs of process-induced strains during curing of thick glass/epoxy laminate plate: experimental results and numerical modelling. *Wind Energy* 2013;16(8):1241–57. <http://dx.doi.org/10.1002/we.1550>.
- [65] Baran I, Cinar K, Ersoy N, Akkerman R, Hattel JH. A review on the mechanical modeling of composite manufacturing processes. *Arch Comput Methods Eng* 2017;24:365–95. <http://dx.doi.org/10.1007/s11831-016-9167-2>.
- [66] Simon SL, Mckenna GB, Sindt O. Modeling the evolution of the dynamic mechanical properties of a commercial epoxy during cure after gelation. *J Appl Polym Sci* 2000;76:495–508. [http://dx.doi.org/10.1002/\(SICI\)1097-4628\(20000425\)76:4<495::AID-APP7>3.0.CO;2-B](http://dx.doi.org/10.1002/(SICI)1097-4628(20000425)76:4<495::AID-APP7>3.0.CO;2-B).
- [67] Plazek DJ, Chay I-C. The evolution of the viscoelastic retardation spectrum during the development of an epoxy resin network. *J Polym Sci B* 1991;29(1):17–29. <http://dx.doi.org/10.1002/polb.1991.090290104>.
- [68] Kappel E. Compensating process-induced distortions of composite structures: A short communication. *Compos Struct* 2018;192:67–71. <http://dx.doi.org/10.1016/j.compstruct.2018.02.059>.